Evolution of an atmospheric Kármán vortex street from high-resolution satellite winds: Guadalupe Island case study

Á. Horváth[1], W. Bresky[2], J. Daniels[3], J. Vogelzang[4], A. Stoffelen[4], J. L. Carr[5], D. L. Wu[6], C. Seethala[7], T. Günther[8], and S. A. Buehler[1]

[1]Meteorological Institute, Universität Hamburg, Hamburg, Germany. [2]I. M. Systems Group, Rockville, Maryland, USA. [3]NOAA/NESDIS Center for Satellite Applications and Research, College Park, Maryland, USA. [4]Royal Netherlands Meteorological Institute (KNMI), de Bilt, The Netherlands. [5]Carr Astronautics, Greenbelt, Maryland, USA. [6]NASA Goddard Space Flight Center, Greenbelt, Maryland, USA. [7]Finnish Meteorological Institute, Kuopio, Finland. [8]Department of Computer Science, ETH Zürich, Zürich, Switzerland

Corresponding author: Ákos Horváth (akos.horvath@uni-hamburg.de, hfakos@gmail.com)

Key Points:

- Novel high spatial and temporal resolution satellite winds enable the study of quasiperiodic island wake flows
- Wind retrievals show anticyclonic vorticity decaying faster than cyclonic vorticity in the lee of Guadalupe Island
- Asymmetric vorticity decay suggests atmospheric Kármán vortex street has 3D rather than 2D structure

Abstract

Vortex streets formed in the stratocumulus-capped wake of mountainous islands are the atmospheric analogues of the classic Kármán vortex street observed in laboratory flows past bluff bodies. The quantitative analysis of these mesoscale unsteady atmospheric flows has been hampered by the lack of satellite wind retrievals of sufficiently high spatial and temporal resolution. Taking advantage of the cutting-edge Advanced Baseline Imager, we derived km-scale cloud-motion winds at 5-minute frequency for a vortex street in the lee of Guadalupe Island imaged by Geostationary Operational Environmental Satellite-16. Combined with Moderate Resolution Imaging Spectroradiometer data, the geostationary imagery also provided accurate stereo cloud-top heights. The time series of geostationary winds, supplemented with snapshots of ocean surface winds from the Advanced Scatterometer, allowed us to capture the wake oscillations and measure vortex shedding dynamics. The retrievals revealed a markedly asymmetric vortex decay, with cyclonic eddies having larger peak vorticities than anticyclonic eddies at the same downstream location. Drawing on the vast knowledge accumulated about laboratory bluff body flows, we argue that the asymmetric island wake arises due to the combined effects of Earth's rotation and Guadalupe's non-axisymmetric shape resembling an inclined flat plate at low angle of attack. The asymmetric vortex decay implies a three-dimensional wake structure, where centrifugal or elliptical instabilities selectively destabilize anticyclonic eddies by introducing edge-mode or core-mode vertical perturbations to the clockwise-rotating vortex tubes.

1 Introduction

Flow past a circular cylinder is a classic problem in fluid dynamics. In an unstratified fluid and nonrotating reference frame, the wake pattern is determined solely by the Reynolds number *Re*. For $Re > \sim 50$, vortices with alternate senses of rotation are shed from alternate sides of the cylinder. As these counterrotating vortices are advected downstream, they form a vortex street of two rows arranged in a staggered configuration as illustrated in Figure 1. For $Re < \sim 190$, vortex shedding is strictly periodic and two dimensional with no vertical (spanwise) variations in the flow. For $\sim 190 < Re < \sim 260$, however, vortex shedding transitions from a laminar regime to a three-dimensional regime as streamwise and transverse vorticity structures develop in addition to the primary spanwise vortices. At higher *Re*, the fine-scale three dimensionality of the wake becomes increasingly disordered, but quasiperiodic coherent vortex shedding is observed even in highly turbulent laboratory flows with *Re* of the order of 10^6 (Williamson, 1996).

Although vortex streets were first photographed by Henri Bénard during his laboratory investigations of vortex spacing (Bénard, 1908a, 1908b), much to his chagrin the phenomenon became associated almost exclusively with Theodore von Kármán, who made two important contributions to the relevant aerodynamic knowledge (von Kármán, 1911, 1912; von Kármán & Rubach, 1912). One, he connected the momentum carried by the vortex system with wake drag. Two, he performed linear stability analysis of a simplified model comprising an infinite train of point vortices embedded in an inviscid fluid and showed that all vortex configurations are unstable, except for one specific staggered configuration with an aspect ratio—distance between vortex rows divided by inter-vortex spacing in one row—of $H/L = 0.281$, which is neutrally stable. Measurements of vortex streets in viscous fluids later found that the actual aspect ratio hardly ever assumes this theoretical value, but rather it increases with downstream distance due to turbulent diffusion, varying from 0.15 to 0.45 and also having a slight dependence on *Re* (Bénard, 1926a,

1926b, 1927; Matsui, 1981). Nevertheless, the vortex pattern sketched in Figure 1 is now universally referred to as the Kármán vortex street in recognition of Kármán's fundamental theoretical insights.

Visible band satellite images often show spectacular trains of vortices in the cloudy wake of mountainous islands, which bear a striking resemblance to patterns observed behind cylinders in low Reynolds number (Re < ~300) laboratory flows—see the fluid motion albums of Samimy et al. (2003) and Van Dyke (1982). These atmospheric vortex streets consist of mesoscale eddies in a well-mixed boundary layer capped by a temperature inversion and are made visible by streaklines in stratocumulus clouds acting as tracer. The eddies span the entire boundary layer as revealed by their sea surface imprints in Synthetic Aperture Radar (SAR) images (Li et al., 2000, 2008). As such, atmospheric vortex streets differ from their laboratory cousins in several important aspects. First and foremost, they develop in a stratified atmosphere on a rotating Earth, which necessitates the introduction of the Froude number Fr and the Rossby number Ro as additional control parameters besides Re. Furthermore, the height to width aspect ratio and the sidewall slope of relatively flat—and often not even axisymmetric—islands are much smaller than those of long cylinders used as obstacles in the laboratory. Finally, while experimental setups go to great lengths to ensure low-turbulence, steady, and uniform upstream flow, such ideal conditions are never achieved in the atmosphere even in the most stable meteorological situations.

Whether atmospheric vortex streets are close physical analogues of laboratory ones or there is only a superficial morphological similarity between these two systems depends ultimately on the nature of the respective dynamical instabilities, vorticity generation and vortex shedding mechanisms responsible for their formation. Although this topic is beyond the scope of our observational study, we note that significant advances have been made in the understanding of laboratory wake dynamics thanks to sophisticated experiments, direct numerical simulations, and the introduction of new theoretical concepts such as global or local and absolute or convective instability. The modern view of the phenomenon describes the onset of vortex shedding at the critical Re = ~50 as a self-excited limit-cycle oscillation (Hopf bifurcation) with the periodic vortex street in the near wake being the saturated end product of a time-amplified global instability (Provansal et al., 1987; Provansal, 2006; Williamson, 1996).

Since Bénard and Kármán's pioneering work a century ago, hundreds of papers have been published on laboratory wake vortices behind bluff bodies (reviewed partly by the excellent two-volume monograph of Zdravkovich, 1997). In contrast, their atmospheric counterparts have attracted considerably less attention due mainly to observational limitations—numerical modeling studies are not surveyed in our paper. Although island vortex streets have been photographed from a number of spacecraft, only the geometric aspect ratio and the vortex shedding frequency have so far been estimated from satellite imagery (Chopra, 1973; Chopra & Hubert, 1965; Hubert & Krueger, 1962; Jensen & Agee, 1978; Lyons & Fujita, 1968; Thomson et al., 1977; Tsuchiya, 1969; Zimmerman, 1969). The most comprehensive past study is that of Young and Zawislak (2006), which derived aspect ratio statistics for 30 vortex streets based on Moderate Resolution Imaging Spectroradiometer (MODIS) images. They found that the aspect ratio of atmospheric vortex streets does follow geometric similarity theories but, much like in laboratory flows, it differs considerably from Kármán's analytical prediction. The measured values were larger, with a mean

111 of 0.42 and a 95% confidence interval of 0.36–0.47 for island vortex streets having a straight
112 centerline.

113 The spaceborne measurement of atmospheric vortex street dynamics however has been out
114 of reach, because the spatial and temporal resolution of operational satellite wind products is still
115 too coarse to retrieve the small-scale wake flow. Existing cloud-motion wind algorithms are based
116 on 1–5 km pixel resolution imagery acquired every 10–100 minutes and use a large tracking box
117 of 26×26–72×72 km^2 (Horváth et al., 2017). Higher temporal and higher spatial resolution
118 sampling is needed to advance the understanding of atmospheric processes in turbulent
119 environments, as highlighted by a review of current remote sensing capabilities (Geerts et al.,
120 2018). Recently developed research-quality wind datasets now offer enhanced resolutions capable
121 of resolving the vortex street wind field. For example, Horváth (2013) demonstrated that 4.4-km
122 resolution stereo cloud-motion winds from the Multiangle Imaging SpectroRadiometer (MISR)
123 could successfully capture the flow and vorticity field of a vortex street in the lee of Jan Mayen
124 Island. Ocean surface winds from the Advanced Scatterometer (ASCAT) resampled on a 6.25-km
125 grid were also shown to well represent the finer details of island wakes including those of a
126 Madeira vortex street, in good agreement with near-coincident 4.4-km cloud-level MISR winds
127 (Nunalee et al., 2015; Vogelzang, 2016; Vogelzang et al., 2017).

128 The current paper reports on the latest improvements in satellite retrievals of small-scale
129 geophysical flows enabled by the enhanced capabilities of the Advanced Baseline Imager (ABI)
130 onboard the Geostationary Operational Environmental Satellite-R (GOES-R) series (Schmit et al.,
131 2017). The ABI provides visible band imagery at a spatial and temporal resolution of 0.5 km and
132 5 minutes over the continental United States (CONUS) scan sector, which includes Guadalupe
133 Island off Baja California. The operational GOES-R wind product contains 7.5-km resolution
134 cloud-motion vectors every 15 minutes (Bresky et al., 2012; Daniels et al., 2010). Internally,
135 however, the algorithm also computes 2.5-km resolution local motion vectors by the nested
136 tracking of 5×5-pixel sub-scenes. Our study takes advantage of these local motion vectors, whose
137 frequency we have also increased to 5 minutes, to investigate an atmospheric Kármán vortex street
138 observed by GOES-16 in the lee of Guadalupe on 9 May 2018. We also exploit a novel MODIS–
139 GOES joint wind product that offers accurate stereo cloud-top heights and semi-independent wind
140 validation data (Carr et al., 2019). Unlike polar-orbiter retrievals providing only snapshots, high
141 temporal resolution geostationary data can capture the oscillation of the wake. We use ABI local
142 cloud-motion vectors over an 8-hr daytime period, combined with two early morning ASCAT
143 surface wind snapshots, to characterize the evolution of the vortex street wind field including the
144 downstream advection and decay of vorticity. To our knowledge, this is the first demonstration of
145 the spaceborne measurement of atmospheric vortex shedding.

146 The paper is organized as follows. Section 2 describes the satellite winds, atmospheric
147 reanalysis fields, other auxiliary data used as well as the calculation of basic flow parameters.
148 Section 3 gives an overview of the meteorological situation at Guadalupe Island on 9 May 2018,
149 determines vortex street geometry, and illustrates GOES-16 and ASCAT retrievals of the vortex
150 street wind field. Section 4 contains a quantitative analysis of the wake's temporal evolution.
151 Finally, section 5 summarizes our results and provides an outlook on the further potential of high
152 spatial and temporal resolution satellite winds for the characterization of unsteady geophysical
153 flows.
154

155 **2 Materials and Methods**

156 **2.1 Wind Datasets**

157 **2.1.1 GOES-16 Local Cloud-Motion Vectors**

158 Our primary data, the GOES-16 local cloud-motion vectors (or "local winds") were
159 calculated using a simplified version of the operational GOES-R Derived Motion Winds (DMW)
160 algorithm (Bresky et al., 2012; Daniels et al., 2010). The simplified version involved use of only
161 the feature tracking portion of the GOES-R DMW algorithm. The local motion winds were not
162 assigned heights as is the case in the operational version, limited quality control was performed on
163 the output, and the tracking was done using image pairs instead of image triplets, in order to
164 increase the spatial coverage and temporal frequency of the retrievals. Winds were extracted from
165 multiple 0.5-km resolution ABI band 2 (0.64 μm visible red band) image pairs separated by a 5-
166 minute time interval, starting at 14:32 UTC and ending at 22:37 UTC. Retrievals were generated
167 every 5 minutes over a 602×602-pixel domain encompassing Guadalupe and its wake down to
168 26°N latitude. A 5×5-pixel (~2.5×2.5 km^2) sub-scene was centered on each pixel in this domain
169 and then tracked forward in time by minimizing the sum-of-squared-difference (SSD) similarity
170 measure between the target image sub-scene and the search image sub-scene. Because our research
171 application is more noise-tolerant than numerical weather prediction (NWP) data assimilation
172 systems, the only quality constraint placed on the raw local motion vectors was that each matching
173 sub-scene had to meet a correlation threshold of 0.8 with the initial target sub-scene.
174

175 **2.1.2 MODIS–GOES-16 3D Cloud-Motion Vectors**

176 We also used data from a novel MODIS–GOES joint wind retrieval algorithm (Carr et al.,
177 2019), which provides horizontal wind vectors with geometric height assignments derived from
178 the stereo tracking of cloud patterns in a triplet of consecutive GOES-16 CONUS scenes and a
179 single MODIS granule. The *Terra* and *Aqua* overpasses yielded two snapshots of the wind field at
180 18:12 UTC and 21:22 UTC. The algorithm is based on red band imagery (ABI band 2, MODIS
181 band 1) as it offers the finest spatial resolution in both systems, 0.5 km and 0.25 km at the
182 respective subsatellite points. Feature templates are taken from the central repetition of the GOES-
183 16 triplet and matched to the other two repetitions 5 minutes before and after, providing the
184 primary source of velocity information. The GOES-16 feature template is then matched to the
185 MODIS granule which is observed from a different perspective, providing the stereoscopic height
186 information. The apparent shift in the pattern from each match, modeled pixel times, and satellite
187 ephemerides feed the retrieval model to enable the simultaneous solution for a wind vector and its
188 geometric height. These joint MODIS–GOES-16 retrievals, hereafter referred to as "3D winds",
189 are derived using 8×8 km^2 templates sampled every 2 km. As such, they have a slightly coarser
190 resolution than the GOES-16 "local winds" described previously. At the same time, the larger
191 template and use of GOES-16 image triplets rather than image pairs lead to visually less noisy,
192 smoother retrievals.
193

2.1.3 ASCAT Ocean Surface Wind Vectors

The Advanced Scatterometer (ASCAT) is a C-band scatterometer carried by the MetOp satellites. Here we used data from ASCAT-A and ASCAT-B, which at the time of our case study were flying half an orbit apart in the same polar orbit with a separation time of ~50 min. ASCAT is a VV (vertical transmit and vertical receive) polarized C-band radar with six fan beam antennas, three at each side of the satellite. Two beams look forward at 45° azimuth with respect to the satellite moving direction, two look cross-track at 90° azimuth, and two backward at 135° azimuth. The radar cross section of the ocean surface is thus measured from three directions in two swaths of about 550 km width (Figa-Saldaña et al., 2002). The ASCAT Wind Data Processor (AWDP) is the standard software for deriving near real-time ocean surface wind vectors from the radar measurements on 25-km and 12.5-km operational grids (KNMI, 2013). In this study, full resolution radar cross sections from the European Organization for the Exploitation of Meteorological Satellites (EUMETSAT) were processed with AWDP using a finer grid spacing of 6.25 km. Although the retrievals have a true spatial resolution of ~17 km, the resulting wind field is oversampled to prevent information loss (Nyquist sampling) and hence the 6.25 km product shows considerably more detail than the coarser resolution operational products (Vogelzang et al., 2017).

We further note that ASCAT measures stress-equivalent winds at 10 m height, derived assuming a near-neutral wind profile in the surface layer (de Kloe et al., 2017). These 10-m winds differ from cloud-motion winds due to the height difference and ocean drag. For example, for a typical aerodynamic roughness of 0.1 mm, near-surface friction velocity of 0.2 m s^{-1}, and 10-m wind of 6 m s^{-1}, the corresponding wind at 1 km height is ~40% faster. This height scaling directly applies to vorticity as well, assuming a constant diameter vortex, and therefore ASCAT wind speeds and vorticity are substantially lower than cloud-motion wind speeds and vorticity.

2.1.4 Processing of the Wind Datasets

All three wind products were regridded onto the same Universal Transverse Mercator (UTM) grid covering our study domain with a spacing of 6.3 km to match the spacing of the coarsest ASCAT data. To reduce noise, each UTM gridbox was assigned the median of the wind vectors it contained. The presence of occasional outliers affected mostly the highest resolution GOES-16 local motion vectors, but for consistency the median filter was applied to the other wind datasets as well. The vertical (spanwise) component of relative vorticity ζ was then calculated from the horizontal wind components using standard finite difference methods (see e.g. Belmonte & Stoffelen, 2019). As additional noise reduction, the regridded and median-filtered data fields were also smoothed with a 3×3-gridbox averaging window.

The original north-south (N-S) and east-west (E-W) wind components were converted to the more fitting streamwise V and transverse U wind components by rotating the coordinate system hourly to align its x-axis with the upstream wind taken from ERA5 (C3S, 2017). This conversion was only approximate, because the upstream wind direction and thus the direction of vortex shedding changed during the day, resulting in a curved vortex street centerline. As a result, the upstream wind direction at any given time was representative of the streamwise (vortex advection) direction only in the near wake but could deviate from it in the far wake.

2.2 ASTER Global Digital Elevation Model

The topography of Guadalupe Island is characterized by the Advanced Spaceborne Thermal Emission and Reflection Radiometer (ASTER) Global Digital Elevation Model Version 2 (GDEM V2) derived from stereo image pairs (NASA/METI/AIST/Japan Spacesystems & U.S./Japan ASTER Science Team, 2009). The ASTER GDEM is distributed in 1°×1° tiles with elevation data posted on a 1 arc-second (~30 m at the equator) grid and has an overall accuracy of ~17 m (Meyer et al., 2011). Combining the GDEM with ERA5 wind and temperature profiles allowed us to calculate the crosswind island diameter at inversion base level, which is the length scale that determines vortex spacing. As shown in Figure 2, Guadalupe's shape is not an approximately axisymmetric cone typical of volcanic peaks (e.g. Jan Mayen and Gran Canaria), but rather resembles an elongated inclined flat plate. The effects of such a shape on the flow are twofold. First, it makes the crosswind island diameter vary considerably with wind direction. Second, it naturally defines a leading edge and trailing edge relative to the upstream wind. In Figure 2 we plotted the "mass density" ellipse fitted to Guadalupe, which clearly indicates that under the prevailing northwesterly winds the northern and southern shores act as the leading and trailing edge, respectively. The angle of attack α, defined as the angle between the upstream wind vector and the major axis of the fitted ellipse, varied between 9° and 32° in our case. As we discuss in section 4, vortex shedding behind an inclined flat plate at low angle of attack is distinct from that behind a circular cylinder.

2.3 MODIS and VIIRS Imagery

Vortex street geometry (vortex spacing and aspect ratio) was determined from Moderate Resolution Imaging Spectroradiometer (MODIS) and Visible Infrared Imaging Radiometer Suite (VIIRS) 0.64 μm red band images. The advantages of polar-orbiter imagery over geostationary imagery are better resolution and minimized image distortion due to the curvature of the Earth. The MODIS *Terra*, VIIRS *Suomi National Polar-Orbiting Partnership* (*Suomi NPP*), and MODIS *Aqua* observed the vortex street at 18:12 UTC, 20:17 UTC, and 21:22 UTC, respectively. The images used were obtained from the NASA Worldview application in an equirectangular map projection with a pixel resolution of 0.25 km.

2.4 Basic Flow Parameters

2.4.1 Reynolds Number

In a nonrotating unstratified fluid, the nature of the wake only depends on the Reynolds number, which is the dimensionless ratio of inertial force to viscous force. The Reynolds number is defined as

$$Re = UD/\nu, \tag{1}$$

where U is the upstream velocity, D is the obstacle (cylinder) diameter, and ν is the kinematic viscosity of the fluid (generally water in laboratory experiments). For atmospheric vortex streets U is of O(1-10) m s^{-1} and $D = D_{inv}$, the crosswind island diameter at inversion base, is of O(1-10)

km. Using the kinematic viscosity of air ν_{air}, which is of O(10^{-5}) m^2 s^{-1}, would yield an exceedingly large Re of O(10^8-10^{10}) implying extremely turbulent conditions.

However, the cloud patterns of atmospheric vortex streets resemble the more laminar patterns observed in laboratory flows with Re < ~300 (see the photographs in Samimy et al., 2003 and Van Dyke, 1982). In order to achieve a semblance of similarity between natural and laboratory conditions, one must invoke the use of the eddy viscosity in the determination of Re for atmospheric vortex streets. The eddy viscosity ν_E is at least five orders of magnitude larger than ν_{air}, however, its appropriate value for atmospheric flows is still debated—a topic not pursued any further in this paper. Suffice it to say, the eddy viscosity approach behaves relatively poorly for large-eddy coherent structures and it allows, at most, only qualitative comparisons between geophysical and laboratory phenomena as pointed out by Boyer and Davies (2000).

2.4.2 Froude Number

The Froude number is the dimensionless ratio of flow inertia to an external field. Although originally introduced in naval architecture to formulate the resistance experienced by partially submerged vessels moving through water, the parameter was also found relevant in the description of stratified atmospheric flows—in which case it is the ratio of inertial force to buoyancy force. There are various formulas for the Froude number (Heinze et al., 2012; Leo et al., 2016) and here we use the one based on the dividing streamline concept of Snyder et al. (1985). The dividing streamline at height h_c separates the air parcels that go over from those that go around the obstacle. The flow above h_c is three-dimensional near the obstacle with a significant vertical component. Below h_c, however, flow splitting leads to quasi two-dimensional streamlines in horizontal planes.

For the atmosphere where wind speed and stratification generally vary with height z, Snyder et al. (1985) derived an implicit expression which can be solved for h_c by iteration:

$$\frac{1}{2}U^2(h_c) = \int_{h_c}^{h_m} N^2(z)(h_m - z)\,dz. \quad (2)$$

Here $U(z)$ is the ERA5 upstream wind speed profile, h_m = 1,298 m is the peak height of Guadalupe, and

$$N(z) = \left(\frac{g}{\theta}\frac{\partial\theta}{\partial z}\right)^{1/2} \quad (3)$$

is the Brunt–Väisälä frequency, with $g = 9.81$ m s^{-2} being the gravitational acceleration and $\theta(z)$ being the ERA5 upstream potential temperature profile. Equation (2) assumes that all horizontal kinetic energy is converted into potential energy and thus provides the lowest possible dividing streamline, which in reality might be found at a somewhat higher level.

Etling (1989) showed that the dividing streamline height obtained above for vertically varying atmospheric wind speed and stratification profiles can be converted to a Froude number that facilitates comparison with laboratory flows under constant upstream velocity and constant stratification:

$$Fr = 1 - h_c/h_m. \quad (4)$$

Laboratory experiments with three-dimensional obstacles in stably stratified flows found spanwise vortex shedding only for $Fr < 0.4$ (Boyer et al., 1987; Brighton, 1978; Hunt & Snyder, 1980), a condition also met by the four atmospheric vortex street cases with available radiosonde profiles that were analyzed by Etling (1989). This restriction on the static stability of the flow requires that $h_c > 0.6h_m$, that is the quasi two-dimensional split-flow regime must cover at least 60% of the vertical extent of the island (~779 m for Guadalupe).

2.4.3 Rossby Number

In the study of rotating fluids, one more dimensionless dynamical parameter has to be introduced, which usually is the Rossby number. The Rossby number is the ratio of inertial force to Coriolis force, defined as

$$Ro = U/fD = U/2D\Omega \sin\phi, \tag{5}$$

where U is the upstream velocity, $D = D_{inv}$ is the crosswind island diameter at inversion base, and $f = 2\Omega \sin\phi$ is the Coriolis parameter, with $\Omega = 7.29 \times 10^{-5}$ s^{-1} being the rate of Earth's rotation and $\phi = 29.03°$ being Guadalupe's latitude.

Thus, for the general case of a stratified rotating fluid a basic set of independent dimensionless control parameters consists of Re, Fr, and Ro. Alternatively, the Ekman number Ek, the ratio of viscous force to Coriolis force, can be used instead of the Reynolds number, in which case $Re = Ro/Ek$ is not an independent parameter any longer.

2.4.4 Strouhal Number

Although not a control parameter, the Strouhal number is an essential dimensionless quantity in the description of oscillating flows. It can be considered a normalized shedding frequency, defined as

$$St = D/TU, \tag{6}$$

where U is the upstream velocity, $D = D_{inv}$ is the crosswind island diameter at inversion base, and T is the shedding period between two consecutive like-rotating vortices. The importance of St stems from the fact that a similarity relationship was observed between St and Re by several laboratory studies, allowing the identification and categorization of distinct flow regimes. Roshko (1954) found for a circular cylinder that St increases steadily with Re from 0.120 to 0.205 for $50 < Re < 300$ and then St asymptotes to the value of 0.210 for $300 < Re < 10^4$. The behavior of St and the definition of flow regimes for even higher Re are reviewed in Williamson (1996).

The Strouhal number for an inclined flat plate, which is a better first-order model of Guadalupe than a cylinder or a cone, has also been studied albeit less extensively (see Rostami et al., 2019 and references therein). The St based on the projected plate width shows a complicated behavior with Reynolds number and angle of attack. Some investigators found a near constant value of $St \approx 0.148$ (Fage and Johansen, 1927; $30° < \alpha < 90°$) or $St \approx 0.17$ (Yang et al., 2012; $20° < \alpha < 30°$, Re = 1,000). Others observed St decreasing with α from 0.18 to 0.14 (Lam & Leung, 2005; $20° < \alpha < 30°$, Re = 5,300). In contrast, the latest study found St increasing sharply from

0.02 at $\alpha = 5°$ to 0.17 at $\alpha = 50°$ and then remaining constant at higher angles (Rostami et al., 2019; $Re = 10^4$–10^5). What emerges robustly from all these studies, however, is that the *St* values for an inclined flat plate correspond to the $Re < 200$ regime of a circular cylinder and stay below the asymptotic value of 0.21.

3 Kármán Vortex Street in the lee of Guadalupe on 9 May 2018

3.1 Meteorological Conditions

Satellite imagery showed a well-developed Kármán vortex street in the cloudy wake of Guadalupe on 9 May 2018. Supplementary animation S1 compiled from GOES-16 band 7 (3.9 μm) and band 2 (0.64 μm) images revealed coherent vortex shedding during the entire day. Although the nighttime shortwave (band 7) infrared brightness temperatures have coarser resolution (2 km) and less contrast than daytime visible reflectances, they still clearly capture the formation and downstream advection of vortex pairs. In fact, vortex shedding was observed throughout 7–9 May and also on 11 May with a vortex-free weak wake pattern in between on 10 May indicating relatively uniform atmospheric conditions favorable to vortex formation over several days. The animated images demonstrate the excellent geolocation of ABI data, but also hint at the sporadic presence of very thin high-level clouds that could hamper the tracking of low-level clouds and thus introduce noise in the wind retrievals.

The hourly ERA5 potential temperature and wind speed profiles upstream of Guadalupe are plotted in Figure 3. The diurnal variation of the most relevant meteorological and flow parameters is also tabulated in Table 1. The marine boundary layer had a well-mixed subcloud layer capped by a strong temperature inversion with a weaker stably stratified layer above and thus exhibited the typical conditions for atmospheric vortex streets. The inversion base was near 350 m in the morning and near 570 m in the afternoon and evening. Wind speed varied between 7 and 12 m s^{-1} with the lowest values occurring in the early hours and showed only a slight increase with height below the mountain peak. The dividing streamline height fluctuated somewhat but was mostly above the 779 m threshold for Guadalupe. Consequently, the Froude number was close to or distinctly below the critical value of 0.4, especially after 12 UTC. Given the uncertainties in ERA5 profiles and considering that h_c calculated from equation (2) was likely a slight underestimate, the Froude number did indicate atmospheric conditions conducive to coherent vortex shedding all day long.

The upstream wind direction and thus, the direction of vortex shedding, increased from 311° at 04–05 UTC to 334° at 15–17 UTC and then decreased to 322° at 22 UTC. The relatively large (23° and 12°) directional swings of these northwesterly winds are apparent in the satellite image loop too. For example, vortex shedding in the near wake as well as the advection of earlier-shed vortices in the far wake shifted noticeably to the east after 17 UTC, as the more westerly background flow introduced an increased zonal wind component. The westerly turn of background winds also resulted in two consecutive anticyclonic vortices being pushed close together and

thereby weakening each other (vortices V2 and V4 in later figures). Such interaction between two successive like-rotating vortices in the same row would not happen under steady uniform flow.

The crosswind island diameter varied systematically with inversion base height and wind direction (see Table 1). Inversion base height had the slightly larger effect, although the changing wind direction also caused significant variations in D_{inv} due to Guadalupe's non-axisymmetric shape. The combined effect of these two parameters produced a factor of two variation in D_{inv} during the day (10–22 km). The crosswind island diameter was also mostly responsible for the variations in *Ro*. The Rossby number was consistently well above 1 and varied between 5 and 15, with the lower values occurring early in the morning.

3.2 Vortex Street Geometry

Vortex spacing and vortex street aspect ratio were determined from 0.25-km pixel resolution MODIS *Terra*, VIIRS *Suomi NPP*, and MODIS *Aqua* images spanning a ~3-hr period between 18:12 and 21:22 UTC. The images are plotted in Figure 4 with the centers of the ten vortices identifiable in the earliest MODIS *Terra* image labelled V1–V10 in increasing downstream order. Due to the temporal change in wind direction, wind speed, and crosswind island diameter, all of which had an effect on vortex spacing, shedding frequency, and advection velocity, the vortex street had a rather irregular geometry. Notably, the background flow became more westerly between 17 and 22 UTC, introducing an easterly shift in vortex shedding and advection. This was most apparent for the near-wake vortices V1–V6, while the far-wake vortices V7–V10 shed much earlier between 06 and 10 UTC under more northerly winds were less affected.

The distortion of vortex street geometry was largest near vortex pair V3–V4. The line connecting the centers of a cyclonic–anticyclonic vortex pair (V1–V2, V5–V6, etc.) typically had a WNW–ESE orientation. The orientation of the V3–V4 pair, in contrast, gradually rotated from WSW–ENE in the MODIS *Terra* image to SW–NE in the MODIS *Aqua* image—at 16:12 UTC, however, V3–V4 still had the usual WNW–ESE orientation. As the background winds turned, the anticyclonic V4 vortex was pushed east and got caught up in the southeasterly flow of the lower part of the succeeding anticyclonic V2 vortex, which dragged it northwestward relative to its cyclonic companion the V3 vortex (see also supplementary animation S1). In fact, the much larger and stronger V2 severely weakened and eventually absorbed V4 such that by 22:07 UTC V4 was not identifiable as a separate local peak in the vorticity field.

In order to avoid the most severe distortions, geometric parameters were only calculated for the three southernmost vortex triplets t1 = (V6, V7, V8), t2 = (V7, V8, V9), and t3 = (V8, V9, V10). The vortex street centerline, obtained by fitting a third-order polynomial to the intervortex midpoints of vortices V5–V10, had an upper segment with considerable curvature and eastward shift caused by the faster easterly advection of the V5–V6 pair. The centerline segment corresponding to vortices V7–V10, on the other hand, was consistently linear and showed a much smaller eastward shift.

As given in Table 2, the aspect ratio *H/L* of vortex triplets t1 and t2 increased sharply in time, because the transverse spacing *H* increased and the streamwise spacing *L* decreased. The t1 and t2 aspect ratios varied between 0.50 and 0.80 and were far outside the 95% confidence interval of 0.36–0.47 obtained by Young and Zawislak (2006) for regular atmospheric vortex streets. The

aspect ratio of t3, which was the triplet least affected by changes in the background flow, however showed good temporal consistency and agreed well with the results of Young and Zawislak (2006).

3.3 Vortex Street Wind Field

3.3.1 ASCAT Surface Winds

The vortex street and the corresponding ocean surface winds at the ASCAT-A overpass time are shown in Figure 5. Lower resolution, reduced contrast, and presence of high-level clouds made it more difficult to discern low-level cloud structures in GOES-16 band 7 nighttime images compared to daytime band 2 images. Nevertheless, the characteristic "mushroom" patterns formed by counterrotating vortex dipoles were still recognizable, especially in the depth map rendition of the brightness temperatures. The vortex street had a curved centerline because the vortices furthest downstream were shed under more northerly winds on 8 May.

The surface winds showed flow splitting coupled with deceleration on the windward side of the island and acceleration zones on the eastern and western flanks, characterized by higher shear and "cornering" winds 2-3 m s^{-1} faster than the background flow. In the lee of the island, a meandering wake of reduced wind speeds and fluctuating wind directions was clearly visible down to 27.5°N. The maximum speed reduction was ~3 m s^{-1} that was accompanied by a ~45° maximum turn in wind direction, both of which gradually diminished downstream. In the vorticity field, eight local peaks could be unambiguously associated with the four vortex pairs seen in the band 7 image. Peak vorticity generally decreased with increasing distance from the island.

As discussed in the next section, the wake effect—speed reduction, oscillations in wind direction, magnitude of vorticity—was stronger and observable considerably further downstream in GOES-16 daytime cloud-motion winds. The coarser resolution of ASCAT retrievals and ocean drag were definitely major reasons for a less pronounced wake and smaller vorticity values. It should be noted, however, that the Froude number was larger at 04–05 UTC (Fr = 0.42–0.43) than after 14 UTC (Fr < 0.4), indicating slightly less favorable conditions for vortex formation in the early hours of the day. In addition, the upstream wind was the most westerly (311°) and consequently the angle of attack was the highest (32°) at the ASCAT observation times, which might have also contributed to a weaker and less southwardly extended wake. Results for the ASCAT-B overpass (not shown) were similar but with the wake shifted further to the east.

We note that Kilpatrick et al. (2019) reported systematic climatological wind errors near coastal mountains in certain scatterometer wind products. The AWDP-processed winds used here have a 180° wind direction ambiguity, but this is generally resolved by the AWDP 2D variational ambiguity removal procedure, which uses empirically-derived spatial structure functions (Vogelzang and Stoffelen, 2012, 2018). In our experience, island lee vortices are captured well by the KNMI ASCAT products, which yield physically consistent wind structures.

3.3.2 GOES-16 Local Winds

Hourly snapshots of GOES-16 local wind vectors between the MODIS *Terra* and MODIS *Aqua* overpasses are plotted in Figure 6, while the variation of local winds over the entire 8-hr period between 14:37 and 22:32 UTC is given every 5 minutes in supplementary animation S2.

The local winds were somewhat noisy and had coverage gaps before 16:00 UTC, probably caused by the presence of thin high-level clouds. Later on, however, there were only occasional speed or direction outliers in the retrievals. The wake signature extended all the way down to 26°N. Flow splitting and deceleration on Guadalupe's windward side and lobes of acceleration on its flanks were also apparent at cloud level. The maximum speed reduction in the wind shadow was ~5 m s^{-1}. Note that the background flow south of Guadalupe was spatially nonuniform as winds were stronger west of the wake than east of the wake—and they also became more westerly after 17 UTC (see Table 1). These spatial and temporal variations in background wind speed and direction introduced a westerly crossflow through the vortex street.

Wind direction within the wake changed by up to 90° at the western rim of cyclonic and eastern rim of anticyclonic vortices, often in association with a zone of acceleration similar to the one on the flanks of the island. The locations of the largest swings in the wind coincided with local minima or maxima in vorticity and the magnitude of the swings generally decreased with downstream distance. Counterclockwise turns in wind direction (decreases in angle) were larger than clockwise turns in wind direction (increases in angle) due to the westerly crossflow. The wind oscillations lead to alternating bands of positive ("westerly") and negative ("easterly") transverse (cross-street) jets, the former again being more prominent than the latter. A westerly jet runs between the bottom of a cyclonic vortex and the top of the preceding anticyclonic vortex, while an easterly jet runs between the bottom of an anticyclonic vortex and the top of the preceding cyclonic vortex. Because of the added westerly crossflow, "easterly" jets had only a weak easterly absolute wind component and typically showed a more northerly orientation. The transverse jets advected downstream with the vortices. For example, the westerly jet located at ~28°N (between 117°W and 118°W) in the MODIS *Terra* image advected down to ~27.6°N (and also further to east) by the time of the MODIS *Aqua* overpass, following the movement of vortex pair V5–V6 shown in Figure 4.

Snapshots of the corresponding streamwise wind component are plotted in Figure 7 with its 8-hr temporal evolution given in supplementary animation S3. The streamwise component showed clearly the wind shadow of Guadalupe with speed reductions up to 5 m s^{-1} in the wake. It had local minima at the locations of the five westerly jets. However, the local minima corresponding to what would have been easterly jets under uniform mean flow conditions were missing, because the westerly crossflow gave these opposing jets a more northerly orientation and thus an increased streamwise wind component.

The oscillating nature of the wake could perhaps be best seen in the transverse wind component plotted in Figure 8 and supplementary animation S4. The transverse wind field exhibited alternating bands of positive and negative values at the locations of the opposing cross-street jets, with the streamwise distance between bands of the same sign regulated by the vortex shedding frequency. Note that the midpoint of the diverging color palette in Figure 8 was shifted from 0 to +1.5 m s^{-1} to account for the westerly crossflow and aid visualization. The regular pattern of the ten alternating bands was somewhat broken by the interaction of the V2 and V4 vortices caused by a change in the shedding direction, as described in section 3.1. This resulted in the corresponding positive and negative bands being distorted into a more circular shape and ending up at approximately the same axial location rather than following each other along the streamwise axis. Also note that several of the bands showed the transverse wind being the strongest near the end points of a cross-street jet and weaker in between, which is the classic pattern in laboratory

flows. The formation and downstream advection of the transverse wind bands was nicely captured in the supplementary animation.

Snapshots of the vertical component of relative vorticity are plotted in Figure 9, while its 8-hr temporal evolution is given in supplementary animation S5. The magnitude of vorticity calculated from cloud-motion winds was a factor of ~2 larger than that calculated from ASCAT surface winds (cf. Figure 5d). This difference was due mostly to the higher spatial resolution of GOES-16 retrievals and ocean drag affecting ASCAT retrievals, although the effect of temporal changes in the atmospheric state—e.g. slightly more favorable conditions for vortex formation after 14 UTC as indicated by the Froude number—could not be ruled out. The plots show the V2 vortex gradually absorbing the V4 vortex, the latter of which almost completely disappeared by 22:02 UTC both in the vorticity maps and visible satellite images. Most importantly, the vorticity calculations revealed an asymmetric downstream vortex decay with cyclonic trailing-edge vortices being stronger than anticyclonic leading-edge vortices at the same axial location. This asymmetry between the counterrotating vortices, which could also be seen in ASCAT retrievals, is further discussed and quantified in section 4.3.

3.3.3 GOES-16 3D Winds

The GOES-16 3D winds and the derived vorticity are plotted in Figure 10 for the MODIS *Terra* overpass. Results for the MODIS *Aqua* overpass (not shown) were of similar quality. As described in section 2.1.2, the 3D winds are representative of a somewhat larger area (8×8 km^2 vs. 2.5×2.5 km^2) and longer averaging time (10 min vs. 5 min) than the local winds, which explains most of the differences between the two products. Because of the larger image template and Guadalupe's location close to the edge of the CONUS sector, the coverage of 3D winds did not extend as far west as that of local winds. The 3D wind retrievals were smoother and exhibited less pronounced minima and maxima. For example, the magnitude of local minima in the streamwise component and the magnitude of local maxima in the transverse component, that is the intensity of the westerly jets, as well as the strength of the individual vortices were all slightly reduced compared to the higher resolution local winds. Nevertheless, the comparison statistics tabulated in Table 3 indicated a good overall agreement between the datasets within 5%. The 3D winds had a slight fast bias due to the less marked wind shadow and showed marginally smaller differences for the E-W component than the N-S component. Although the two wind products were derived from the same imagery and hence were not fully independent, their consistency still enhanced our confidence in both.

The salient feature of the joint wind retrieval is the stereoscopic height assignment, which is potentially more accurate than traditional infrared brightness temperature-based height assignment techniques. Examining the retrievals for cloud-free feature templates over land provides a useful self-consistency validation, since the algorithm is expected to return near-zero winds and heights close to the terrain elevation. This is a technique pioneered with MISR (Horváth, 2013; Lonitz & Horváth, 2011; Moroney et al., 2002). The *Aqua* granule provided ample ground-

point retrievals, which showed a median height retrieval error of 28.3 m and a standard deviation of 66.9 m.

The stereo cloud-top heights (CTHs) showed a cloud layer between 600 and 900 m encountering the island peak and revealed that vortex formation left the vertical structure of the cloud layer largely undisturbed. The median stereo CTH was nearly the same at the two MODIS overpass times, 742 m and 726 m respectively. Brightness temperature-based CTHs from the collection 6 MOD06 and MYD06 operational MODIS products were biased slightly high: 900–1000 m upstream and 900–1200 m downstream. The stereo CTHs were more consistent with a 570 m inversion base height (see section 3.1) and a typical marine stratocumulus thickness of 200–300 m (Stevens et al., 2007).

4 Wake Flow Dynamics

4.1 Observed Vortex Shedding Mechanisms

Visual analysis of the high spatial and temporal resolution animations of GOES-16 band 2 imagery (S1) and derived vorticity (S5) enabled us to draw a basic sketch of vortex shedding behind Guadalupe. The animations revealed different vortex formation mechanisms at the trailing edge and the leading edge. Flow separation at the trailing edge is unaffected by Guadalupe's elongated shape and thus the counterclockwise-rotating vortices simply roll up and shed directly from the trailing edge. At the leading edge, however, the island itself acts as a long after-body object for flow separation. The clockwise-rotating vortices generated at the leading edge first extend along the streamwise direction and develop into a large recirculation region on the eastern flank of Guadalupe that remains attached to the island for some time. The growth and eventual detachment of this clockwise recirculation region as a fully-fledged leading-edge vortex is controlled largely by the development of the next counterclockwise-rotating trailing-edge vortex. As a result, leading-edge vortices shed into the wake at an axial location near the trailing edge too. This implies that at the same streamwise location, leading-edge vortices have undergone a longer birth and more diffusion than trailing-edge vortices, which might explain the smaller anticyclonic vorticities downstream (more on this in section 4.3). These vortex formation processes observed behind Guadalupe are in excellent qualitative agreement with the asymmetric vortex shedding found behind an inclined flat plate both in large-eddy simulations (LES, Breuer & Jovičić, 2001) and wind tunnel experiments (Lam & Leung, 2005), further confirming the flat plate as a better model for Guadalupe than the circular cylinder or cone.

4.2 Temporal Variation of Wind Components

The temporal variation of wind speed and the various wind components during the 8-hr daytime period is plotted every 5 minutes in Figure 11 for one downstream location outside and one inside the wake. The background flow was sampled near the western edge and central latitude of our domain (27.685°N, 118.166°W), while the wake was sampled at the western end point of the first transverse jet closest to the island (28.596°N, 118.047°W), where wind oscillations were the largest.

Wind speed showed a ~2 m s^{-1} variation during this time period, generally increasing after 16:32 UTC. The wind speed deficit between the selected main flow and wake locations was also

~2 m s^{-1}. Because the wake was sampled near the edge of rather than the middle of the wind shadow, the speed reduction was smaller than the maximum value of ~5 m s^{-1} found earlier. The westerly crossflow was indicated clearly by the increasing E-W component of the main flow after 16:32 UTC (Figure 11a), which was due both to the strengthening and the westerly turn of the background winds. The corresponding N-S component also increased slightly with increasing wind speed. Aligning the coordinate system hourly with the ERA5 upstream wind vector accounted for the turning wind direction to first order and resulted in a transverse component with much reduced fluctuations around zero (Figure 11b). Coordinate system rotation alone could not completely eliminate the crossflow and thus the transverse component still exhibited a small variation, switching from slight negative to slight positive values at 16:32 UTC. Apart from these relatively small, smooth, and slow variations, however, the wind field did not exhibit any observable oscillations outside the wake.

In contrast, winds within the wake experienced quasiperiodic oscillations of significant magnitude. Given the driving northwesterly winds, the E-W and N-S components both showed oscillations, the magnitude of which was slightly larger for the former than the latter (Figure 11c). The oscillations were the clearest and had the largest amplitude in the transverse component, while the streamwise component showed the smallest temporal variations with no obvious periodicity. Rotating the coordinate system mostly accounted for the westerly crossflow in the first half of our study period and hence the transverse component showed positive and negative fluctuations of comparable magnitude (±4–5 m s^{-1}). After 20:00 UTC, however, there was a distinct shift towards positive values in the transverse wind as a result of the uncorrected crossflow.

The 8-hr time period encompassed two full vortex shedding cycles and some. By visual analysis of the GOES-16 image loops, we estimated the shedding period between two consecutive like-rotating vortices varying between 2 and 4 hr during the entire day. With the diurnal variations in upstream velocity and crosswind island diameter, this yielded a Strouhal number between 0.09 and 0.18 with the higher values occurring early in the morning. This *St* range was considerably below the 0.21 asymptotic value for a circular cylinder.

As revealed by the oscillations in the transverse wind component (Figure 11d) and also confirmed by the GOES-16 animations, the shedding period gradually increased from 2.2 hr to 3.7 hr between 15 and 22 UTC, corresponding to a decrease in *St* from ~0.12 to ~0.09. During the same time period the crosswind island diameter increased and the upstream wind speed slightly decreased, leading to an overall increase in *Re*. For a circular cylinder, *St* increases steadily with *Re* in the regime below the asymptotic value. The observed decrease in *St* with *Re* is therefore inconsistent with the classic similarity relationship for a circular cylinder. On the other hand, the angle of attack also increased between 15 and 22 UTC, and *St* decreasing with α qualitatively agrees with Lam & Leung (2005)'s findings for an inclined flat plate. However, a note of caution is in order here, because there is no consensus yet on the *St*–α relationship among experimental studies and its dependence on *Re* is also largely unexplored, as discussed in section 2.4.4. In our case *Re* and α varied simultaneously, which prevents disentangling their independent effects.

It is instructional at this point to examine the time-averaged wind and vorticity fields, plotted in Figure 12. The wind vectors show flow splitting with deceleration on the windward northern shores, a prominent leading-edge lobe of acceleration on the eastern flank, and a reattachment region just south of the island at 118°W. Downstream the reattachment region, the wind vectors indicate a NW–SE orientation with approximate parallel streamlines as the velocity

642 oscillations averaged out to a large degree. The shape of the reduced-wind-speed zone, however,
643 still revealed the meandering of the wake over time. Towards the south of the island, the time-
644 averaged winds suggested a counterclockwise recirculation zone associated with the trailing edge.

645 For comparison, the time-averaged velocity field behind a circular cylinder with periodic
646 Kármán vortex shedding shows two symmetrically placed counterrotating standing vortices
647 attached to the cylinder and streamlines parallel to the main flow past the reattachment point
648 (Goharzadeh & Molki, 2015). The time-averaged flow behind an inclined flat plate is similar, but
649 the clockwise recirculation region at the leading edge is considerably larger than the anticlockwise
650 recirculation region at the trailing edge (Breuer & Jovičić, 2001; Yang et al., 2012). Interestingly,
651 this flow pattern with two steady counterrotating recirculation regions is characteristic of the
652 laminar steady regime ($5 < Re < 50$) that occurs between "creeping flow" ($Re < 5$) and laminar
653 periodic vortex shedding ($50 < Re < 190$). The lack of the clockwise recirculation zone in our time-
654 averaged wind field might have been caused by the uncorrected westerly crossflow or retrieval
655 uncertainties in the largely cloud-free area immediately east of the island.

656 The vorticity map corresponding to the time-averaged wind vectors (Figure 12b) outlined
657 the positive and negative vorticity generation regions on the western and eastern flanks of the
658 island. The tendency towards stronger cyclonic than anticyclonic vortices *downstream* Guadalupe
659 was apparent here too, as the tongue of elevated positive vorticities extended further south than
660 the corresponding negative contour line of the same magnitude. The vorticity generation areas
661 *near* the island, however, showed the opposite asymmetry in strength. The peak vorticity of the
662 anticyclonic region associated with the leading edge was -5.73×10^{-4} s^{-1}, while that of the cyclonic
663 region associated with the trailing edge was 4.67×10^{-4} s^{-1}. Higher peak vorticity production near
664 the leading edge than the trailing edge but stronger cyclonic than anticyclonic vortices further
665 downstream agrees again with the experimental results of Lam & Leung (2005) for an inclined flat
666 plate.
667

668 **4.3 Asymmetric Vortex Decay**

669 The vorticity maps in Figure 9 have already indicated visually that (i) the strength of
670 individual vortices decreased with downstream distance and (ii) the decrease was faster for
671 anticyclonic (negative) vorticity than for cyclonic (positive) vorticity. In this section, we quantify
672 the asymmetric vorticity decay and discuss its potential causes. The downstream (axial) distance
673 was measured from Guadalupe's center and was normalized by the crosswind island diameter at
674 inversion base height: $x^* = x/D_{inv}$. We used vorticity calculated from GOES-16 local winds for the
675 time period 15:32–20:32 UTC, which excluded the noisiest earlier retrievals as well as later
676 retrievals most affected by the crossflow (see Figure 11).

677 Peak vorticity as a function of x^* is plotted in Figure 13, separately for the vorticity
678 production regions on the flanks of the island (plus signs) and for individual vortices advecting
679 downstream (filled circles). A statistical summary of the results is also given in Table 4. Echoing
680 the findings for the time-averaged winds, the mean peak vorticity was higher in the anticyclonic
681 vorticity production region than in the cyclonic vorticity production region: -6.19×10^{-4} s^{-1} vs
682 5.61×10^{-4} s^{-1}. The asymmetry, however, was the opposite for vortices shed into the wake. The
683 average peak vorticity of anticyclonic vortices was not only smaller than that of cyclonic vortices,

684 -3.67×10^{-4} s^{-1} vs 4.74×10^{-4} s^{-1}, but the streamwise linear decay rate of anticyclonic vorticity was
685 also twice as high as that of cyclonic vorticity: 0.19×10^{-4} s^{-1} / D_{inv} vs -0.09×10^{-4} s^{-1} / D_{inv}.

686 At $x^* = 10–11$ there was an anomalous drop in both negative vorticity (to -2.5×10^{-4} s^{-1}) and
687 positive vorticity (to 3.5×10^{-4} s^{-1}), which corresponded to the V3–V4 vortex pair located at the
688 geometrically most distorted portion of the vortex street (see Figure 4 and section 3.2). As
689 discussed previously, the larger anticyclonic V2 vortex started to absorb and weaken the smaller
690 anticyclonic V4 vortex due to the westerly turn of the background winds. The westerly crossflow
691 also pushed the cyclonic V3 vortex close to the V4 vortex (in fact the V3–V4 pair had the smallest
692 transverse separation of all vortex pairs), resulting in the overlap of the adjacent eddy cores and
693 partial cancellation of vorticity of opposite signs. Excluding the V3–V4 pair from the analysis,
694 however, did not change our finding of a markedly asymmetric downstream vorticity decay.

695 Note that ASCAT-A/B ocean surface winds showed the same cyclonic-anticyclonic
696 asymmetry in vortex strength and downstream decay rate, although in a much smaller sample. The
697 magnitude of vorticities and the difference between them were considerably smaller than those for
698 GOES-16 cloud-motion winds, due to the coarser resolution of the scatterometer data and ocean
699 drag effects. In contrast, decay rates per D_{inv} were higher because the crosswind island diameter
700 was a factor of 2 larger at the ASCAT overpass times than during the GOES-16 observations.
701 Decay rates per 100 km, however, were fairly comparable between the instruments (see Table 4).

702 Another measure of vortex street intensity is the peak transverse wind in cross-street jets,
703 which is plotted as a function of x^* in Figure 13b. Similar to peak vorticity, positive jets were on
704 average stronger than negative jets, although this discrepancy was due partly or perhaps mostly to
705 the uncorrected westerly crossflow—an ~1 m s^{-1} crossflow could easily eliminate the observed
706 asymmetry. Here we note that while a spatially uniform crossflow biases the transverse wind
707 component, it does not bias the vorticity. Regardless, the intensity of transverse jets clearly
708 decreased as the wind oscillations dampened downstream, suggesting a nonlinear decay with the
709 decline being steeper in the near wake and then tapering off in the far wake.

710 In the classic Lamb-Oseen vortex model, peak vorticity decreases inversely with time,
711 which translates to a hyperbolic spatial decay along the streamwise axis for a roughly constant
712 vortex advection speed. Such a vortex model was used successfully to describe the viscous decay
713 of 2D vortices shed by a circular cylinder as observed in both laboratory experiments and direct
714 numerical simulations (Ponta, 2010). In our retrievals, the peak transverse wind could be fitted
715 reasonably well with a hyperbola, but the peak vorticity followed a linear decay. The different
716 decay functions might have been the result of using *raw* transverse winds but *smoothed* vorticities
717 in the analysis. Deviations from the 2D Lamb-Oseen vortex model in a significantly 3D wake or
718 variations with *Re* could also lead to more linear decay laws (Hamid et al., 2015).

719 To recap, the general decay of vortices can be explained by the viscous diffusion of
720 vorticity. In a manner analogous to the diffusion of heat, vorticity spreads into the flow as vortices
721 advect in the wake. The size of eddies also increases downstream due to diffusion, a tendency that
722 can be seen in Figure 4 too, leading to the gradual overlapping of viscous cores and cancellation
723 of vorticity of opposite signs. To account for the asymmetry in the cyclonic and anticyclonic decay
724 rates, however, requires considering the effects of Earth's rotation or obstacle shape on the flow.

725 For a circular cylinder, asymmetric vortex decay could only be achieved in both laboratory
726 experiments and numerical simulations by the inclusion of moderate background rotation. In a
727 rotating environment the Rossby number is an additional control parameter. When $Ro \ll 1$

(geostrophic regime), the strong background rotation tends to two-dimensionalize the flow and thus stabilize columnar vortices against perturbations. Taylor–Proudman theory suggests that in this regime cyclones and anticyclones behave very similarly (Carnevale et al., 1997). In the opposite limit, when $Ro >> 1$, the flow does not feel the rotation and again there is no fundamental difference between cyclones and anticyclones. It is in the intermediate regime with $Ro \geq 1$ where selective 3D destabilization of anticyclonic vortices can occur through various modes of instability.

Boyer & Davies (1982) and Boyer & Kmetz (1983) conducted laboratory investigations of homogeneous flow past a circular cylinder in a rotating water channel. Although they noted clear differences in the flow structure between *f*-plane (constant Coriolis parameter) and β-plane (latitudinally varying Coriolis parameter) as well as between westward and eastward flows, the formation of an asymmetric wake with cyclonic eddies dominating anticyclonic ones was common in all experiments. Carnevale et al. (1997) studied the stability of three-dimensionally perturbed individual vortex tubes in a rotating flow using numerical simulations. They found that for a large but finite Rossby number ($Ro = 5$), even small perturbations lead to the complete breakdown of the anticyclonic vortex through centrifugal instability, while the cyclones remain stable.

Another set of laboratory studies by Afanasyev & Peltier (1998) and Afanasyev (2002) investigated the evolution of an anticyclonic columnar vortex subjected to either centrifugal or elliptical instability. When the vortex is quasi-circular centrifugal instability dominates, which introduces primary perturbations around the edge of the vortex in the form of toroidal rib vortices with mushroom-like cross section. When the vortex is exposed to a strain field and has a more elliptical shape, elliptical instability is dominant. In this case the core of the anticyclone bends in a sinusoidal manner in the plane corresponding to the direction of maximal strain. The competition between centrifugal (edge mode) and elliptical (core mode) instabilities is governed by the magnitude of ellipticity and the Rossby number. Maximum destabilization was found at $Ro = 4$ or 10 for the centrifugal mode and at $Ro = 3$–6 for the elliptical mode.

The experimental work perhaps most pertinent to our case is that of Stegner et al. (2005), which investigated the stability of entire Kármán vortex streets, rather than that of single vortex tubes, in a rotating deep-water layer. They concluded that the breaking of symmetry is primarily caused by core-centered sinusoidal perturbations due to elliptical instability. Cyclonic–anticyclonic asymmetry was observed for $Ro \geq 1.2$ where the vertical wavelength of the perturbations increased with *Ro*. They also found that vorticity decay in coherent vortices comes not only from classic viscous dissipation but also from the direct energy cascade toward small scales induced by the 3D instability. For small Reynolds numbers ($Re \sim 150$), no asymmetry between peak cyclonic and anticyclonic vorticity was detected as standard viscous dissipation dominated. For larger Reynolds numbers ($Re \sim 400$–500), however, viscous dissipation was weaker and selective destabilization of anticyclones was more efficient, resulting in an asymmetric decay. Asymmetric Kármán vortex streets were also observed in a shallow-water configuration more similar to atmospheric flows, where the vertical to horizontal aspect ratio is $<< 1$.

The range of Rossby numbers investigated by the above studies combined is 1–16, which covers our case where *Ro* varied between 5 and 15. Some of these studies even used satellite photos of Guadalupe vortex streets to build a qualitative bridge between laboratory or numerical model results on rotational effects and geophysical flows. The cyclonic-anticyclonic asymmetry is frequently detectable in the visual appearance of vortices in Guadalupe's wake. Anticyclonic

eddies tend to have smaller clear eyes and less well-preserved spiral cloud patterns than cyclonic eddies at the same downstream location, which is apparent in Figure 4 too (e.g. compare the vortices in pairs V1–V2 and V7–V8). The primacy of elliptical instability in causing the wake asymmetry would also imply more elliptically elongated shapes for anticyclones and more circular shapes for cyclones. Because shape perception by a human observer is highly subjective, we defer judgment on this issue until an objective analysis of vortex shapes is conducted in a larger sample.

A factor that has been overlooked consistently in explaining the asymmetric island wake is Guadalupe's non-axisymmetric shape resembling an inclined flat plate. Both laboratory experiments (Lam & Leung, 2005) and numerical simulations (Breuer & Jovičić, 2001; Lam & Wei, 2010; Yang et al., 2012) confirmed that an inclined flat plate at angles of attack encountered in our case (9°–32°) produces inherently asymmetric vortex shedding even without background rotation, although the exact cause of asymmetry is not fully understood yet. Lam and Leung (2005) pointed out that leading edge (anticyclonic) vortices undergo a longer birth before detachment and hence are more diffused with a smaller peak vorticity than trailing edge (cyclonic) vortices at the same axial location. The numerical simulations additionally revealed the significant three-dimensionality of the flow—in fact the laboratory-observed vortex dynamics could not be reproduced in 2D simulations. Braids of streamwise vorticity can form around the primary spanwise Kármán rollers and at certain angles of attack even oblique shedding and vortex dislocations can occur. Such wake instabilities are likely to play a part in the selective destabilization of anticyclonic eddies.

Background rotation and shape effects are present simultaneously in the case of Guadalupe vortex streets and their relative contributions cannot be determined from satellite measurements alone. The excellent qualitative agreement between the vortex formation topologies observed in the laboratory and in satellite imagery, however, strongly suggests that Guadalupe's inclined flat plate shape is an important factor in the development of the asymmetric wake.

5 Summary and Outlook

We investigated the evolution and dynamics of an atmospheric Kármán vortex street observed by GOES-16 in the lee of Guadalupe Island on 9 May 2018. Exploiting the state-of-the-art imaging capabilities of the ABI instrument and the nested tracking algorithm designed specifically for the GOES-R series, we derived cloud-motion winds in the island's wake on a 2.5-km scale every 5 minutes over an 8-hr daytime period. A novel MODIS–GOES joint wind product provided accurate stereo cloud-top heights and semi-independent wind validation data. ASCAT retrievals processed on a fine 6.25-km grid contributed two additional early morning snapshots of ocean surface winds. These high spatial and temporal resolution research-quality winds enabled the quantitative analysis of atmospheric vortex shedding and vortex decay, for the first time from spaceborne observations.

The vortex street developed under atmospheric stratification conducive to coherent vortex shedding. The marine boundary layer had a well-mixed subcloud layer capped by a strong temperature inversion with a weaker stably stratified layer above. The Froude number related to the dividing streamline was typically below the critical value of 0.4, corroborating previous findings. Confirming the quality of the satellite retrievals, the derived wind field around Guadalupe exhibited characteristics expected from laboratory flows past bluff bodies: flow splitting with deceleration on the windward side, lobes of acceleration on the flanks, and an oscillating wake

with transverse jets at quasi-regular intervals set by a vortex shedding period of 2–4 hr. A westerly turn in the background winds during the day introduced slight deviations in the observed flow patterns compared to idealized laboratory results obtained under uniform freestream conditions. The westerly crossflow also distorted the vortex street geometry, leading to a curved centerline and uncharacteristically large aspect ratios at most locations. The aspect ratio in the least-affected far wake, however, showed good temporal consistency, varying between 0.42 and 0.46 and falling within the 95% confidence interval of 0.36–0.47 found for regular atmospheric vortex streets by Young and Zawislak (2006).

Most importantly, both GOES-16 and ASCAT winds revealed an asymmetric island wake with cyclonic eddies having larger peak vorticities than anticyclonic ones at the same downstream location. Vorticity generally decreased with time, that is with downstream distance, due to viscous diffusion but the rate of decrease was a factor of two higher for anticyclones. For a circular cylinder such asymmetric vortex shedding can only occur under the influence of moderate background rotation. When the Rossby number is larger than unity, as was the case for the studied vortex street, anticyclonic vortices can be selectively destabilized by either centrifugal or elliptical instability, depending on the initial shape of the vortices and the rate of rotation. However, non-axisymmetric obstacles can also produce inherently asymmetric wakes even without the presence of background rotation. An inclined flat plate at low angle of attack, which is a good first-order model for Guadalupe under the prevailing northwesterly winds, sheds weaker leading edge (anticyclonic) eddies than trailing edge (cyclonic) eddies, as found by both laboratory experiments and numerical simulations.

Rotational and shape effects act simultaneously on the flow past Guadalupe and their relative contributions can only be determined by future modeling studies, where these two factors can be controlled independently. Nevertheless, the different leading edge and trailing edge vortex formation topologies observed in GOES-16 imagery show excellent qualitative agreement with laboratory results, suggesting that Guadalupe's non-axisymmetric shape does have a substantial influence on the wake. The asymmetric vorticity decay in itself implies a three-dimensional wake structure, because the instabilities that selectively destroy anticyclones produce 3D perturbations either around the edge (centrifugal instability) or in the core (elliptical instability) of the clockwise-rotating vertical vortex tubes.

Cloud-motion winds derived from ABI imagery hold great potential for the further study of unsteady geophysical flows. As demonstrated in this work, the retrievals provided by GOES-16 located at 75°W already show good performance, but GOES-17 now positioned at 135°W offers significantly better views of Guadalupe and thus less noisy wind estimates. Reduced measurement noise will improve the calculation of local differential flow properties such as vorticity, since they require a numerical estimation of derivatives. The high temporal resolution of ABI observations also enables the application of analysis techniques that are well-known in dynamical systems theory, but which have largely been overlooked in applied meteorology.

A first possible approach is to locate material lines, that is sets of particles with exceptional properties, along which the normal separation is maximized over time. These extremal lines are known as hyperbolic Lagrangian coherent structures (LCS; Haller, 2015), which can be approximated through the finite-time Lyapunov exponent (FTLE; Shadden et al., 2005). The FTLE estimates the maximal expansion rate of a virtual sphere in a dynamical system, which is extremal along material boundaries. Depending on whether the expansion is measured in forward-time or backward-time, this gives rise to repellors or attractors in the flow. Such material boundaries are

of great significance in Lagrangian transport analysis, since they divide the domain into compartments of coherent flow behavior that order the flow. For instance, they separate vortices from each other.

An alternative avenue is to process local flow properties from a Lagrangian perspective. Instantaneous properties can be averaged along particle trajectories if they can be assumed to be passively advected with the fluid. This so-called Lagrangian smoothing enforces temporal coherence (Shi et al., 2009). In addition, when averaging the deviation of vorticity from its local neighborhood along trajectories, the resulting Lagrangian-averaged vorticity deviation has a desirable property: similar to the aforementioned LCS, it is invariant to rotations and translations of the frame of reference (Haller et al., 2016). Due to the relativity between observer and the observed feature, this formally guarantees that translating and rotating flow structures can be faithfully extracted (Günther & Theisel, 2018). Analyzing a vector field from the perspective of a local observer that moves with the vortices will enable the application of sophisticated steady-state vortex separation and extraction techniques (Rojo & Günther, 2019). Initial experience with these advanced analysis methods applied to the current Guadalupe vortex street is encouraging and will be presented in a future paper.

Acknowledgments and Data

We acknowledge the use of MODIS and VIIRS imagery from the NASA Worldview application (https://worldview.earthdata.nasa.gov), part of the NASA Earth Observing System Data and Information System (EOSDIS). We also acknowledge the NASA LAADS DAAC for providing the C6 MODIS Atmosphere data (https://ladsweb.modaps.eosdis.nasa.gov). The GOES-16 ABI L1b radiances are available from the NOAA Comprehensive Large Array-data Stewardship System (CLASS) archive (https://www.avl.class.noaa.gov/saa/products/welcome). The ASCAT wind data processor used here has been developed with support of the EUMETSAT NWP Satellite Application Facility (SAF) and the Ocean and Sea Ice SAF. Wind derivatives follow the procedures established in the Copernicus Marine Environment Monitoring Service (CMEMS). The ASTER GDEM Version 2 is a product of Japan's Ministry of Economy, Trade, and Industry (METI) and NASA. The high-resolution GOES-16 and ASCAT wind retrievals derived specifically for this study are available from the Zenodo data repository (https://doi.org/10.5281/zenodo.3534276). The work of Á. Horváth was supported by the German Federal Ministry of Education and Research (BMBF) project HD(CP)2 (contract O1LK1505D). J. Vogelzang thanks Maria Belmonte Rivas of KNMI for explaining how to use the software to calculate divergence and rotation of wind fields.

References

Afanasyev, Ya. D. (2002). Experiments on instability of columnar vortex pairs in rotating fluid. *Geophysical & Astrophysical Fluid Dynamics*, *96*(1), 31–48. https://doi.org/10.1080/03091920290018835

Afanasyev, Ya. D., & Peltier, W. R. (1998). Three-dimensional instability of anticyclonic swirling flow in rotating fluid: Laboratory experiments and related theoretical predictions. *Physics of Fluids*, *10*(12), 3194–3202. https://doi.org/10.1063/1.869846

Belmonte Rivas, M., & Stoffelen, A. (2019). Characterizing ERA-Interim and ERA5 surface wind biases using ASCAT. *Ocean Science, 15*, 831–852. https://doi.org/10.5194/os-15-831-2019.

Bénard, H. (1908a). Étude cinématographique des remous et des rides produits par la translation d'un obstacle. *Comptes rendus de l'Académie des Sciences*, *147*, 970–972.

Bénard, H. (1908b). Formation de centres de giration à l'arrière d'un obstacle en movement. *Comptes rendus de l'Académie des Sciences*, *147*, 839–842.

Bénard, H. (1926a). Sur les lois de la fréquence des tourbillons alternés détachés derrière un obstacle. *Comptes rendus de l'Académie des Sciences*, *182*, 1375–1377.

Bénard, H. (1926b). Sur l'inexactitude, pour liquides réels, de lois théoriques de Kármán relatives à la stabilité des tourbillons alternés. *Comptes rendus de l'Académie des Sciences*, *182*, 1523–1526.

Bénard, H. (1927). Sur les écarts des valeurs de la fréquence alternés à la loi de similitude dynamique. *Comptes rendus de l'Académie des Sciences*, *183*, 20–22.

Boyer, D. L. & Davies, P. A. (1982). Flow past a circular cylinder on a β-plane. *Philosophical Transactions of the Royal Society A: Mathematical, Physical and Engineering Sciences*, *306*(1496), 533–556. https://doi.org/10.1098/rsta.1982.0094

Boyer, D. L. & Kmetz, M. L. (1983). Vortex shedding in rotating flows. *Geophysical & Astrophysical Fluid Dynamics*, *26*(1-2), 51–83. https://doi.org/10.1080/03091928308221763

Boyer, D. L., & Davies, P. A. (2000). Laboratory studies of orographic effects in rotating and stratified flows. *Annual Review of Fluid Mechanics*, *32*(1), 165–202. https://doi.org/10.1146/annurev.fluid.32.1.165

Boyer, D. L., Davies, P. A., Holland, W. R., Biolley, F., & Honji, H. (1987). Stratified rotating flow over and around isolated three-dimensional topography. *Philosophical Transactions of the Royal Society A: Mathematical, Physical and Engineering Sciences*, *322*(1564), 213–241. https://doi.org/10.1098/rsta.1987.0049

Bresky, W., Daniels, J., Bailey, A., & Wanzong, S. (2012). New methods toward minimizing the slow speed bias associated with atmospheric motion vectors. *Journal of Applied Meteorology and Climatology*, *51*(12), 2137–2151. https://doi.org/10.1175/JAMC-D-11-0234.1

Breuer, M. & Jovičić, N. (2001). Separated flow around a flat plate at high incidence: an LES investigation. *Journal of Turbulence*, *2*, N18. https://doi.org/10.1088/1468-5248/2/1/018

Brighton, P. W. (1978). Strongly stratified flow past three-dimensional obstacles. *Quarterly Journal of the Royal Meteorological Society*, *104*(440), 289–307. https://doi.org/10.1002/qj.49710444005

C3S (Copernicus Climate Change Service) (2017). ERA5: Fifth generation of ECMWF atmospheric reanalyses of the global climate . *Copernicus Climate Change Service Climate Data Store (CDS)*, *date of access 2019*. https://cds.climate.copernicus.eu/cdsapp#!/home

Carnevale, G. F., Briscolini, M., Kloosterziel, R. C., & Vallis, G. K. (1997). Three-dimensionally perturbed vortex tubes in a rotating flow. *Journal of Fluid Mechanics*, *341*, 127–163. https://doi.org/10.1017/S0022112097005430

Carr, J. L., Wu, D. L., Wolfe, R. E., Madani, H., Lin, G. G., & Tan, B. (2019). Joint 3D-wind retrievals with stereoscopic views from MODIS and GOES. *Remote Sensing*, *11*(18), 2100. https://doi.org/10.3390/rs11182100

Chopra, K. P. (1973). Atmospheric and oceanic flow problems introduced by islands. In *Advances in Geophysics.* (Vol. 16). New York, NY: Academic Press.

Chopra, K. P., & Hubert, L. F. (1965). Mesoscale eddies in wakes of islands. *Journal of the Atmospheric Sciences*, *22*(6), 652–657. http://dx.doi.org/10.1175/1520-0469(1965)022%3C0652:MEIWOI%3E2.0.CO;2

Daniels, J., Bresky, W., Wanzong, S., Velden, C., & Berger, H. (2010). GOES-R Advanced Baseline Imager (ABI) algorithm theoretical basis document for derived motion winds. *GOES-R Program Office*, 96pp. [Available online at https://www.star.nesdis.noaa.gov/goesr/documents/ATBDs/Baseline/ATBD_GOES-R_Winds_v3.1_Feb2019.pdf.]

de Kloe, J., Stoffelen, A., & Verhoef, A. (2017). Improved Use of scatterometer measurements by using stress-equivalent reference winds. *IEEE Journal of Selected Topics in Applied Earth Observations and Remote Sensing*, *10*(5), 2340–2347. https://doi.org/10.1109/JSTARS.2017.2685242

Etling, D. (1989). On atmospheric vortex streets in the wake of large islands. *Meteorology and Atmospheric Physics*, *41*(3), 157–164. https://doi.org/10.1007/BF01043134

Fage, A., & Johansen, F. C. (1927). On the flow of air behind an inclined flat plate of infinite span. *Proceedings of the Royal Society A: Mathematical, Physical, and Engineering Sciences*, *116*(773), 170–197. https://doi.org/10.1098/rspa.1927.0130

Figa-Saldaña, J., Wilson, J., Attema, E., Gelsthorpe, R., Drinkwater, M., & Stoffelen, A. (2002). The advanced scatterometer (ASCAT) on the meteorological operational (MetOp) platform: A follow on for the European wind scatterometers. *Canadian Journal of Remote Sensing*, *28*(3), 404–412. https://doi.org/10.5589/m02-035

Geerts, B., Raymond, D. J., Grubišić, V., Davis, C. A., Barth, M. C., Detwiler, A., et al. (2018). Recommendations for in situ and remote sensing capabilities in atmospheric convection and turbulence. *Bulletin of the American Meteorological Society*, *99*(12), 2463–2470. https://doi.org/10.1175/BAMS-D-17-0310.1

Goharzadeh, A., & Molki, A. (2015). Measurement of fluid velocity development behind a circular cylinder using particle image velocimetry (PIV). *European Journal of Physics*, *36*(1), 015001. https://doi.org/10.1088/0143-0807/36/1/015001

Günther, T., & Theisel, H. (2018). The state of the art in vortex extraction. *Computer Graphics Forum*, *37*(6), 149–173. https://doi.org/10.1111/cgf.13319

Haller, G. (2015). Lagrangian coherent structures. *Annual Review of Fluid Mechanics*, *47*(1), 137–162. https://doi.org/10.1146/annurev-fluid-010313-141322

Haller, G., Hadjighasem, A., Farazmand, M., & Huhn, F. (2016). Defining coherent vortices objectively from the vorticity. *Journal of Fluid Mechanics, 795*, 136–173. https://doi.org/10.1017/jfm.2016.151

Hamid, A. H. A., Hussam, W. K., Pothérat, A., & Sheard, G. J. (2015). Spatial evolution of a quasi-two-dimensional Kármán vortex street subjected to a strong uniform magnetic field. *Physics of Fluids*, *27*(5), 053602. https://doi.org/10.1063/1.4919906

Heinze, R., Raasch, S., & Etling, D. (2012). The structure of Kármán vortex streets in the atmospheric boundary layer derived from large eddy simulation. *Meteorologische Zeitschrift*, *21*(3), 221–237. https://doi.org/10.1127/0941-2948/2012/0313

Horváth, Á. (2013). Improvements to MISR stereo motion vectors. *Journal of Geophysical Research: Atmospheres*, *118*(11), 5600–5620. https://doi.org/10.1002/jgrd.50466

Horváth, Á., Hautecoeur, O., Borde, R., Deneke, H., & Buehler, S. A. (2017). Evaluation of the EUMETSAT global AVHRR wind product. *Journal of Applied Meteorology and Climatology*, *56*(8), 2353–2376. https://doi.org/10.1175/JAMC-D-17-0059.1

Hubert, L. F., & Krueger, A. F. (1962). Satellite pictures of mesoscale eddies. *Monthly Weather Review*, *90*(11), 457–463. http://dx.doi.org/10.1175/1520-0493(1962)090%3C0457:SPOME%3E2.0.CO;2

Hunt, J. C. R., & Snyder, W. H. (1980). Experiments on stably and neutrally stratified flow over a model three-dimensional hill. *Journal of Fluid Mechanics*, *96*(4), 671–704. https://doi.org/10.1017/S0022112080002303

Jensen, N. O., & Agee, E. M. (1978). Vortex cloud street during AMTEX 75. *Tellus*, *30*(6), 517–523. http://dx.doi.org/10.3402/tellusa.v30i6.10396

Kilpatrick, T., Xie, S.-P., Tokinaga, H., Long, D., & Hutchings, N. (2019). Systematic scatterometer wind errors near coastal mountains. *Earth and Space Science*, *2*. https://doi.org/10.1029/2019EA000757

KNMI (2013). ASCAT wind product user manual. Report SAF/OSI/CDOP/KNMI/TEC/MA/126. [Available online at http://projects.knmi.nl/scatterometer/publications/pdf/ASCAT_Product_Manual.pdf.]

Lam, K. M., & Leung, M. Y. H. (2005). Asymmetric vortex shedding flow past an inclined flat plate at high incidence. *European Journal of Mechanics - B/Fluids*, *24*(1), 33–48. https://doi.org/10.1016/j.euromechflu.2004.05.004

Lam, K. M., & Wei, C. T. (2010). Numerical simulation of vortex shedding from an inclined flat plate. *Engineering Applications of Computational Fluid Mechanics*, *4*(4), 569–579. https://doi.org/10.1080/19942060.2010.11015342

Leo, L. S., Thompson, M. Y., Di Sabatino, S., & Fernando, H. J. S. (2016). Stratified flow past a hill: Dividing streamline concept revisited. *Boundary-Layer Meteorology*, *159*(3), 611–634. https://doi.org/10.1007/s10546-015-0101-1

Li, X., Clemente-Colón, P., & Pichel, W. G. (2000). Atmospheric vortex streets on a RADARSAT SAR image. *Geophysical Research Letters*, *27*(11), 1655–1658. https://doi.org/10.1029/1999GL011212

1022 Li, X., Zheng, W., Zou, C.-Z., & Pichel, W. G. (2008). A SAR observation and numerical study
1023 on ocean surface imprints of atmospheric vortex streets. *Sensors*, *8*(5), 3321–3334.
1024 https://doi.org/10.3390/s8053321

1025 Lonitz, K., & Horváth, Á. (2011). Comparison of MISR and Meteosat-9 cloud-motion vectors.
1026 *Journal of Geophysical Research: Atmospheres*, *116*, D24202.
1027 https://doi.org/10.1029/2011JD016047

1028 Lyons, W. A., & Fujita, T. (1968). Mesoscale motions in oceanic stratus as revealed by satellite
1029 data. *Monthly Weather Review*, *96*(5), 304–314. https://doi.org/10.1175/1520-
1030 0493(1968)096<0304:MMIOSA>2.0.CO;2

1031 Matsui, T. (1981). Flow visualization studies of vortices. *Proceedings of the Indian Academy of*
1032 *Sciences: Engineering Sciences*, *4*(2), 239–257. [Available online at
1033 https://www.ias.ac.in/article/fulltext/sadh/004/02/0239-0257.]

1034 Meyer, D., Tachikawa, T., Kaku, M., Iwasaki, A., Gesch, D., Oimoen, M., et al. (2011). ASTER
1035 Global Digital Elevation Model Version 2 – Summary of validation results. *METI & NASA*,
1036 26pp. [Available online at
1037 https://ssl.jspacesystems.or.jp/ersdac/GDEM/ver2Validation/Summary_GDEM2_validati
1038 on_report_final.pdf.]

1039 Moroney, C., Horváth, Á., & Davies, R. (2002). Use of stereo-matching to coregister multiangle
1040 data from MISR. *IEEE Transactions on Geoscience and Remote Sensing*, *40*(7), 1541-
1041 1546. https://doi.org/10.1109/TGRS.2002.801146

1042 NASA/METI/AIST/Japan Spacesystems, & U.S./Japan ASTER Science Team (2009). ASTER
1043 Global Digital Elevation Model [Data set]. *NASA EOSDIS Land Processes DAAC*.
1044 Accessed 2019-11-08 from https://doi.org/10.5067/ASTER/ASTGTM.002

1045 Nunalee, C. G., Horváth, Á., & Basu, S. (2015). High-resolution numerical modeling of mesoscale
1046 island wakes and sensitivity to static topographic relief data. *Geoscientific Model*
1047 *Development*, *8*(8), 2645-2653. https://doi.org/10.5194/gmd-8-2645-2015

1048 Ponta, F. L. (2010). Vortex decay in the Kármán eddy street. *Physics of Fluids*, *22*(9), 093601.
1049 https://doi.org/10.1063/1.3481383

1050 Provansal, M. (2006). Wake instabilities behind bluff bodies. In *Springer tracts in modern physics.*
1051 *Dynamics of spatio-temporal cellular structures: Henri Bénard centenary review.* (Vol.
1052 207). New York, NY: Springer. https://doi.org/10.1007/b106790

1053 Provansal, M., Mathis, C., & Boyer, L. (1987). Bénard-von Kármán instability: Transient and
1054 forced regimes. *Journal of Fluid Mechanics*, *182*(1), 1–22.
1055 http://dx.doi.org/10.1017/S0022112087002222

1056 Rojo, I. B., & Günther, T. (2019). Vector field topology of time-dependent flows in a steady
1057 reference frame. *IEEE Transactions on Visualization and Computer Graphics*.
1058 https://doi.org/10.1109/TVCG.2019.2934375

1059 Roshko, A. (1954). On the development of turbulent wakes from vortex streets. *Report 1191,*
1060 *National Advisory Committee for Aeronautics*, Washington DC. [Available online at
1061 http://resolver.caltech.edu/CaltechAUTHORS:ROSnacarpt1191.]

1062 Rostami, A. B., Mobasheramini, M., & Fernandes, A. C. (2019). Strouhal number of flat and
1063 flapped plates at moderate Reynolds number and different angles of attack: Experimental
1064 data. *Acta Mechanica*, *230*(1), 333–349. https://doi.org/10.1007/s00707-018-2292-2

1065 Samimy, M., Breuer, K. S., Leal, L. G., & Steen, P. H. (Eds.). (2003). *A gallery of fluid motion*.
1066 Cambridge, United Kingdom: Cambridge University Press.

1067 Schmit, T. J., Griffith, P., Gunshor, M. M., Daniels, J. M., Goodman, S. J., & Lebair, W. J. (2017).
1068 A closer look at the ABI on the GOES-R Series. *Bulletin of the American Meteorological*
1069 *Society*, *98*(4), 681–698. https://doi.org/10.1175/BAMS-D-15-00230.1

1070 Shadden, S. C., Lekien, F., & Marsden, J. E. (2005). Definition and properties of Lagrangian
1071 coherent structures from finite-time Lyapunov exponents in two-dimensional aperiodic
1072 flows. *Physica D: Nonlinear Phenomena*, *212*(3-4), 271–304.
1073 https://doi.org/10.1016/j.physd.2005.10.007

1074 Shi, K., Theisel, H., Hauser, H., Weinkauf, T., Matkovic, K., Hege, H.-C., & Seidel, H.-P. (2009).
1075 Path line attributes - an information visualization approach to analyzing the dynamic
1076 behavior of 3D time-dependent flow fields. In H.-C. Hege, K. Polthier, G. Scheuermann
1077 (Eds.), *Topology-Based Methods in Visualization II*, *Mathematics and Visualization* (pp.
1078 75–88). Berlin, Heidelberg: Springer. https://doi.org/10.1007/978-3-540-88606-8_6

1079 Snyder, W. H., Thomson, R. S., Eskridge, R. E., Lawson, R. E., Castro, I. P., Lee, S. T., Hunt, J.
1080 C. R., & Ogawa, J. (1985). The structure of strongly stratified flows over hills: Dividing
1081 streamline concept. *Journal of Fluid Mechanics*, *152*, 249–288.
1082 http://dx.doi.org/10.1017/S0022112085000684

1083 Stegner, A., Pichon, T., & Beunier, M. (2005). Elliptical-inertial instability of rotating Karman
1084 vortex streets. *Physics of Fluids*, *17*(6), 066602. https://doi.org/10.1063/1.1937348

1085 Stevens, B., Beljaars, A., Bordoni, S., Holloway, C., Köhler, M., Krueger, S., Savic-Jovcic, V., &
1086 Zhang, Y. (2007). On the structure of the lower troposphere in the summertime
1087 stratocumulus regime of the northeast Pacific. *Monthly Weather Review*, *135*(3), 985–
1088 1005. https://doi.org/10.1175/MWR3427.1

1089 Thomson, R. E., Gower, J. F. R., & Bowker, N. W. (1977). Vortex streets in the wake of the
1090 Aleutian Islands. *Monthly Weather Review*, *105*(7), 873–884.
1091 http://dx.doi.org/10.1175/1520-0493(1977)105%3C0873:VSITWO%3E2.0.CO;2

1092 Tsuchiya, K. (1969). The clouds with the shape of Kármán vortex street in the wake of Cheju
1093 Island, Korea. *Journal of the Meteorological Society of Japan Series II*, *47*(6), 457–465.
1094 http://dx.doi.org/10.2151/jmsj1965.47.6_457

1095 van Dyke, M. (1982). *An album of fluid motion*. Stanford, CA: Parabolic Press.

1096 Vogelzang, J. (2016). ASCAT-6.25 validation. NWP SAF Tech. Doc. NWPSAF-KN-TV-009, 80
1097 pp. [Available online at
1098 https://www.nwpsaf.eu/site/download/documentation/scatterometer/reports/ASCAT-
1099 6.25_validation.pdf.]

1100 Vogelzang, J., & Stoffelen, A. (2012). NWP Model Error Structure Functions obtained from
1101 Scatterometer Winds. *IEEE Transactions on Geoscience and Remote Sensing*, *50*(7),
1102 2525–2533. https://doi.org/10.1109/TGRS.2011.2168407

Vogelzang, J., & Stoffelen, A. (2018). Improvements in Ku-band scatterometer wind ambiguity removal using ASCAT-based empirical background error correlations. *Quarterly Journal of the Royal Meteorological Society*, *144*(716), 2245–2259. https://doi.org/10.1002/qj.3349

Vogelzang, J., Stoffelen, A., Lindsley, R. D., Verhoef, A., & Verspeek, J. (2017). The ASCAT 6.25 km wind product. *IEEE Journal of Selected Topics in Applied Earth Observations and Remote Sensing*, *10*(5), 2321–2331. https://doi.org/10.1109/JSTARS.2016.2623862

von Kármán, Th. (1911). Über den Mechanismus des Widerstandes, den ein bewegter Körper in einer Flüssigkeit erfärt. 1. Teil, *Nachr. Ges. Wiss. Göttingen. Math.-Phys. Kl.* (1911) 509–517. Reprinted in *Collected works of Theodore von Kármán* (Butterworth, London, 1956) 1 324–330.

von Kármán, Th. (1912). Über den Mechanismus des Widerstandes, den ein bewegter Körper in einer Flüssigkeit erfärt. 2. Teil, *Nachr. Ges. Wiss. Göttingen. Math.-Phys. Kl.* (1912) 547–556. Reprinted in *Collected works of Theodore von Kármán* (Butterworth, London, 1956) 1 331–338.

von Kármán, Th., & Rubach, H. (1912). Über den Mechanismus des Flüssigkeits und Luftwiderstandes. Phys. Z., 13, 49–59. Reprinted in *Collected works of Theodore von Kármán* (Butterworth, London, 1956) 1 339–358.

Williamson, C. H. K. (1996). Vortex dynamics in the cylinder wake. *Annual Review of Fluid Mechanics*, *28*(1), 477–539. https://doi.org/10.1146/annurev.fl.28.010196.002401

Yang, D., Pettersen, B., Andersson, H. I., & Narasimhamurthy, V. D. (2012). Vortex shedding in flow past an inclined flat plate at high incidence. *Physics of Fluids*, *24*(8), 084103. https://doi.org/10.1063/1.4744982

Young, G. S., & Zawislak, J. (2006). An observational study of vortex spacing in island wake vortex streets. *Monthly Weather Review*, *134*(8), 2285–2294. https://doi.org/10.1175/MWR3186.1

Zdravkovich, M. M. (1997). *Flow around circular cylinders.* (Vols. 1-2). New York, NY: Oxford University Press.

Zimmerman, L. I. (1969). Atmospheric wake phenomena near the Canary Islands. *Journal of Applied Meteorology*, *8*(6), 896–907. http://dx.doi.org/10.1175/1520-0450(1969)008%3C0896:AWPNTC%3E2.0.CO;2

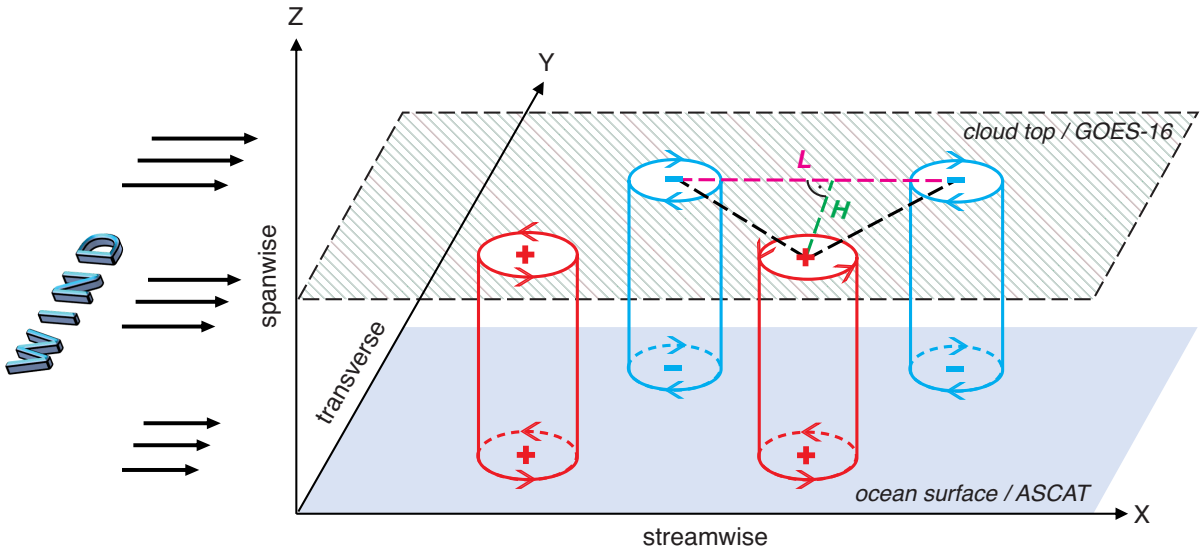

Figure 1. Schematic geometry of an atmospheric vortex street and definition of coordinate axes – the generating mountain is not depicted. The Kármán vortices span the marine boundary layer between the cloud top level and the ocean surface. The vortex street aspect ratio is defined as the transverse distance between the two rows of counterrotating vortices H, divided by the streamwise spacing of like-rotating vortices L. The aspect ratio can be calculated for each triplet of consecutive vortices. The flow at cloud top and the surface is respectively characterized by GOES-16 cloud-motion vectors and ASCAT ocean surface wind vectors. Below a critical Reynolds number of ~190, laboratory flows past a circular cylinder exhibit purely periodic and 2D vortex shedding, as sketched here. Above the critical Reynolds number, however, laboratory vortex shedding transitions into a 3D regime as increasingly intricate streamwise and transverse vorticity structures develop in addition to the primary vertical (spanwise) Kármán vortices.

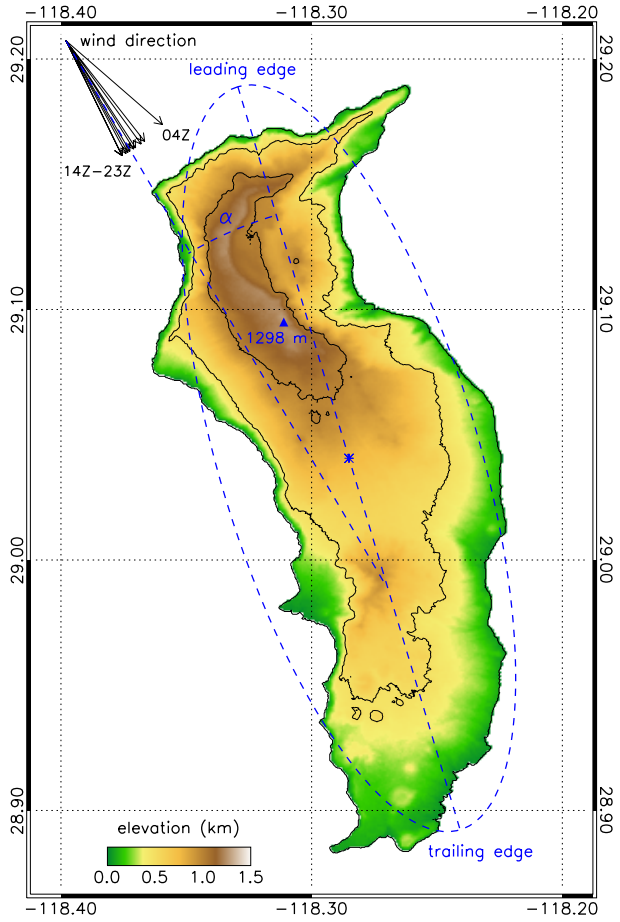

Figure 2. Topography of Guadalupe Island from the ASTER Global Digital Elevation Model (GDEM) Version 2. The black contour lines are drawn at sea level, 0.5 km and 1.0 km and the highest point, Mount Augusta, is marked by the blue triangle. The GDEM was used in conjunction with hourly ERA5 temperature and wind profiles to determine the crosswind island diameter at inversion base height. Black arrows show the ERA5 upstream wind direction at the ASCAT-A/B (04Z-05Z) and GOES-16 (14Z-23Z) retrieval times. The blue dashed outline is the "mass density" ellipse fitted to the island with its major axis oriented at 343.4° and center indicated by the blue asterisk. The angle between the upstream wind vector and the major axis of the ellipse is the angle of attack α. The prevailing northwesterly winds set the northern and southern shores of Guadalupe as the leading and trailing edge.

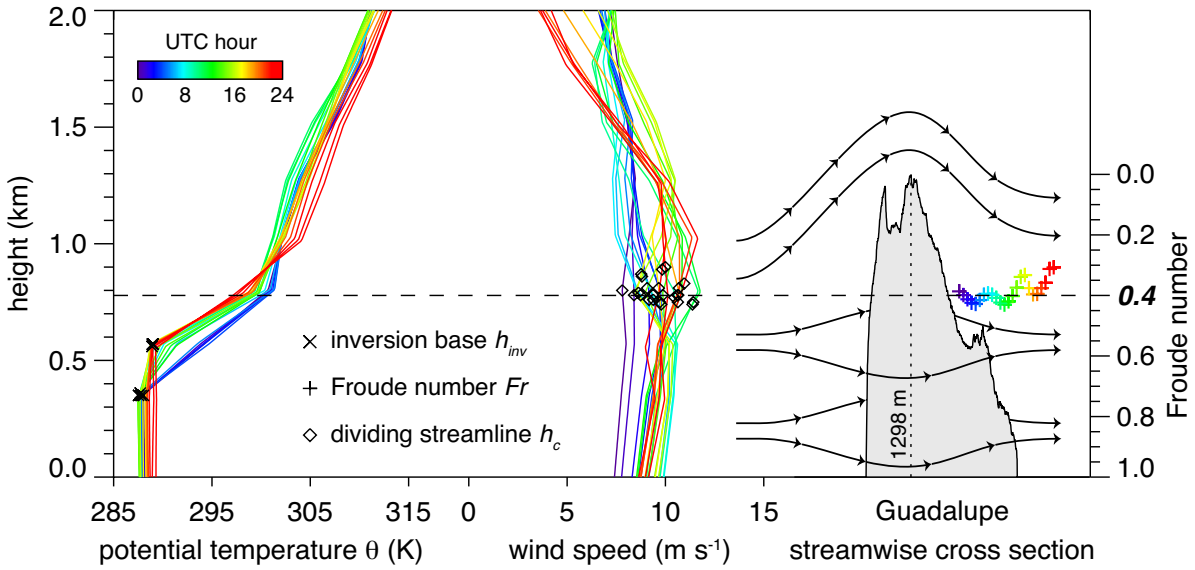

Figure 3. ERA5 vertical profiles of potential temperature θ and wind speed upstream of Guadalupe on 9 May 2018, with UTC hour from 0Z to 23Z being color coded. The height of the inversion base h_{inv} and that of the dividing streamline h_c are respectively marked by crosses and diamonds. Fluid parcels above h_c can flow over the mountain peak, while parcels below h_c tend to pass laterally around the island (flow splitting). The Froude number related to the dividing streamline Fr is plotted with plus signs. For atmospheric vortex street formation Fr is typically below the critical value of 0.4, the corresponding critical dividing streamline height of which is indicated by the dashed line. The cross section of Guadalupe is vertically exaggerated.

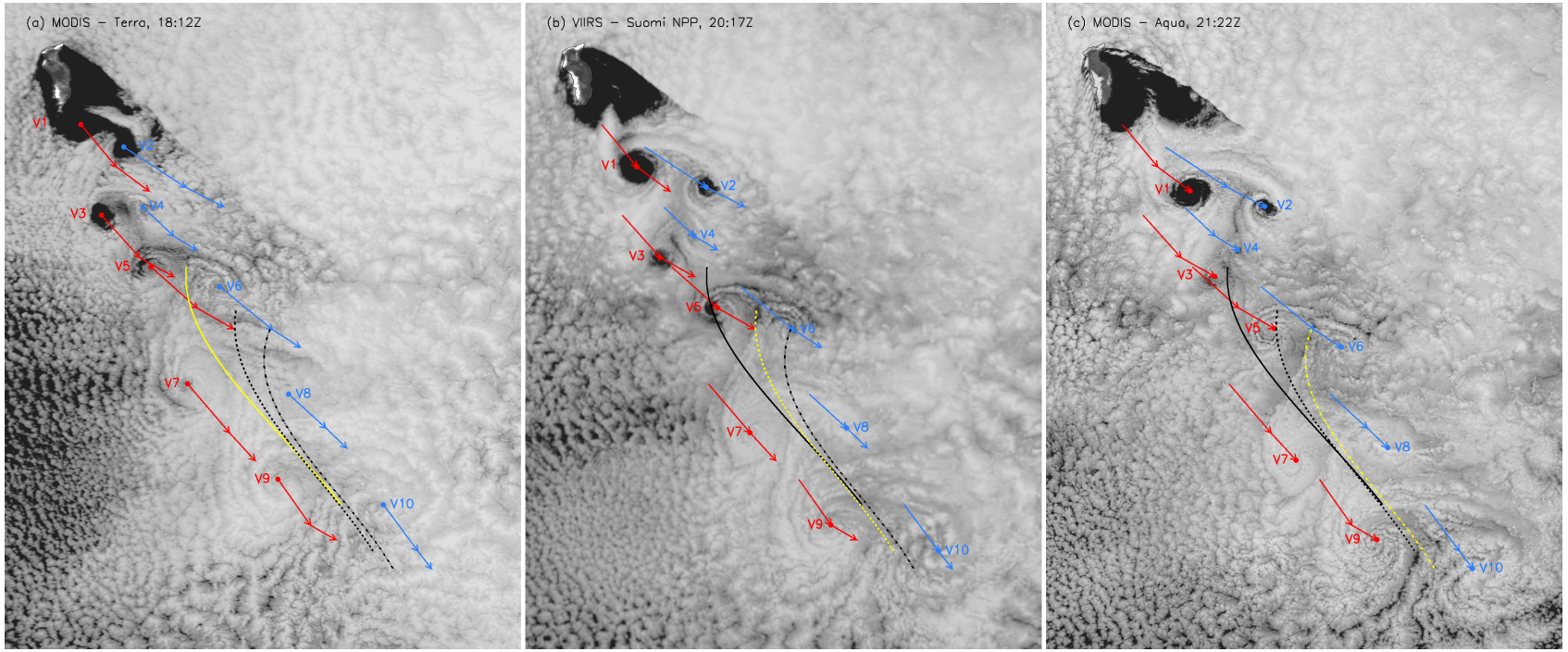

Figure 4. The Kármán vortex street in Guadalupe's wake on 9 May 2018 observed by (a) MODIS *Terra* at 18:12Z, (b) VIIRS *Suomi NPP* at 20:17Z, and (c) MODIS *Aqua* at 21:22Z. Red and blue dots mark the cyclonic and anticyclonic vortex centers in a given image, while the arrows indicate the movement of the vortex centers over the three images. The solid, dashed, and dash-dot-dot lines show the 3rd order polynomial centerline fitted to the locations of vortices V5–V10 respectively at the MODIS *Terra*, VIIRS *Suomi NPP*, and MODIS *Aqua* observation times. The centerline corresponding to a particular image is plotted in yellow.

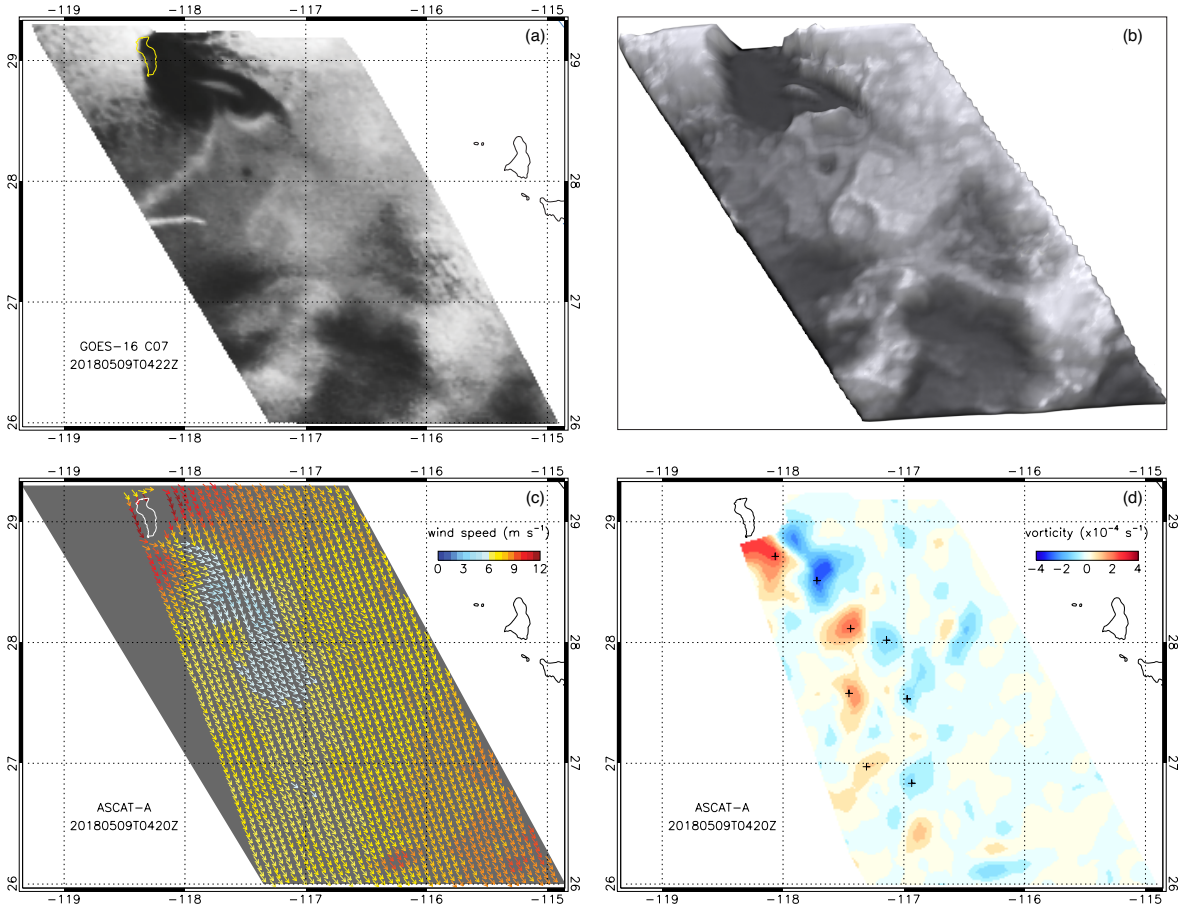

Figure 5. (a) Histogram-equalized grayscale image of GOES-16 channel 7 (3.9 μm) brightness temperatures of the 9 May 2018 Guadalupe vortex street at the ASCAT-A overpass time of 04:20Z, with darker shades representing hotter surfaces. (b) 3D depth map rendition of panel (a) that better accentuates the vortex pair "mushroom" patterns hinted at in the 2D image. The cold and bright high-level cloud streaks near 28°N, 118°W were digitally removed to emphasize the low-level cloud structures. (c) ASCAT-A 6.3 km ocean surface wind vectors colored according to wind speed and (d) the corresponding vorticity field, which was smoothed with a 3×3-gridbox averaging window. The black plus signs in panel (d) mark the locations of vorticity minima and maxima.

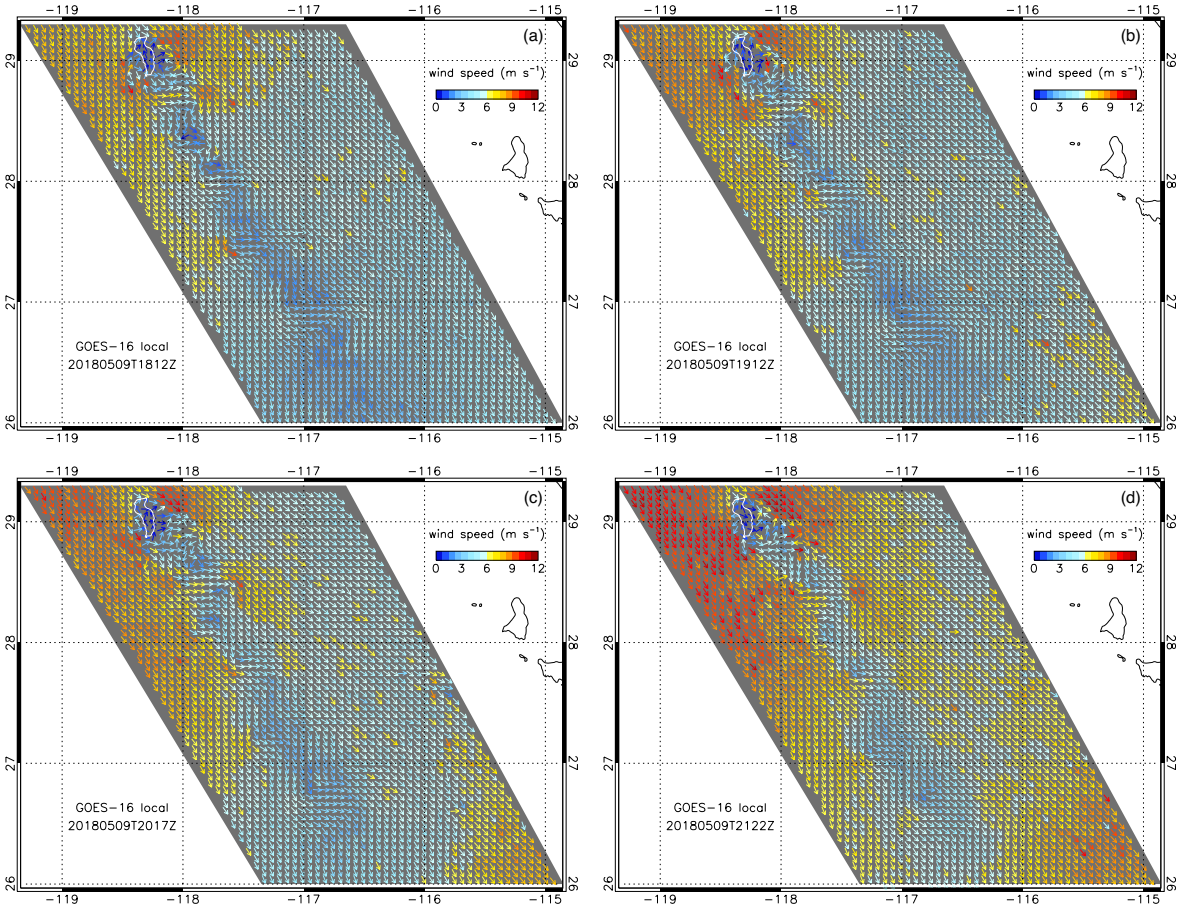

Figure 6. Median-filtered GOES-16 local wind vectors resampled without smoothing on a 6.3-km UTM grid and colored according to wind speed on 9 May 2018 at (a) 18:12Z, (b) 19:12Z, (c) 20:17Z, and (d) 21:22Z. The covered time period is ~3 hr and panels (a), (c), and (d) correspond to the MODIS *Terra*, VIIRS *Suomi NPP*, and MODIS *Aqua* overpass times respectively. The X and Y coordinate axes are aligned with the N-S and E-W directions.

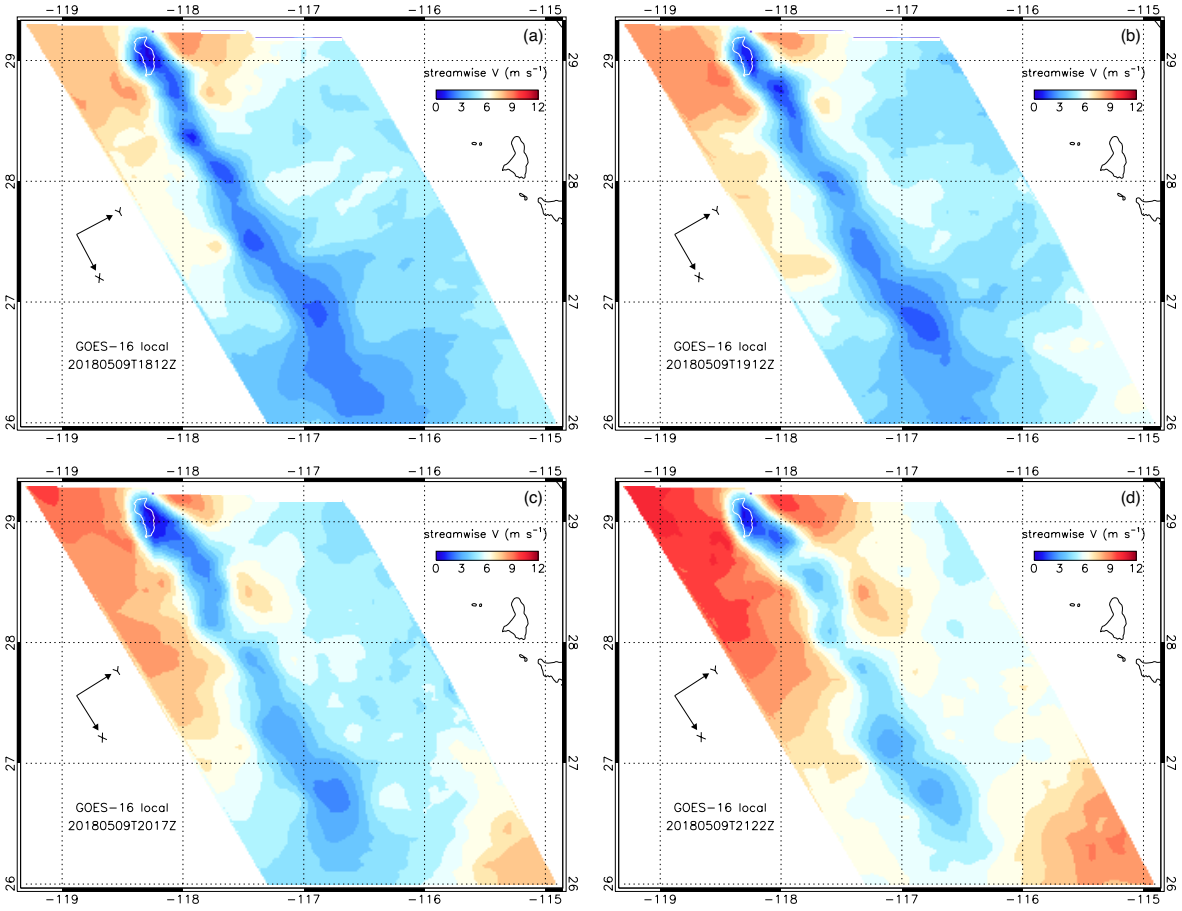

Figure 7. Same as Figure 6, but for the streamwise wind component V smoothed with a 3×3-gridbox averaging window. The X and Y coordinate axes were rotated from the N-S, E-W directions to the streamwise, transverse directions using the ERA5 upstream wind direction.

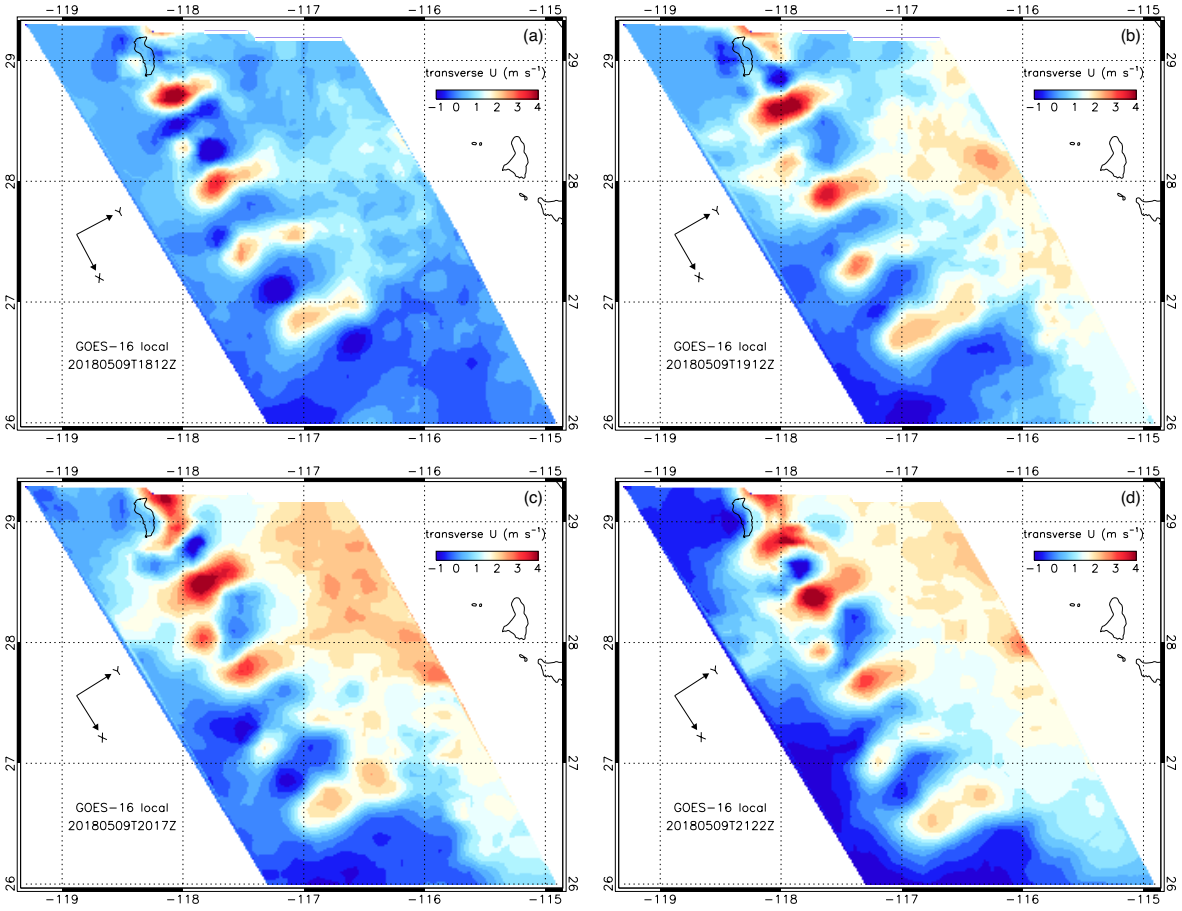

Figure 8. Same as Figure 6, but for the transverse wind component U smoothed with a 3×3-gridbox averaging window. The X and Y coordinate axes were rotated from the N-S, E-W directions to the streamwise, transverse directions using the ERA5 upstream wind direction.

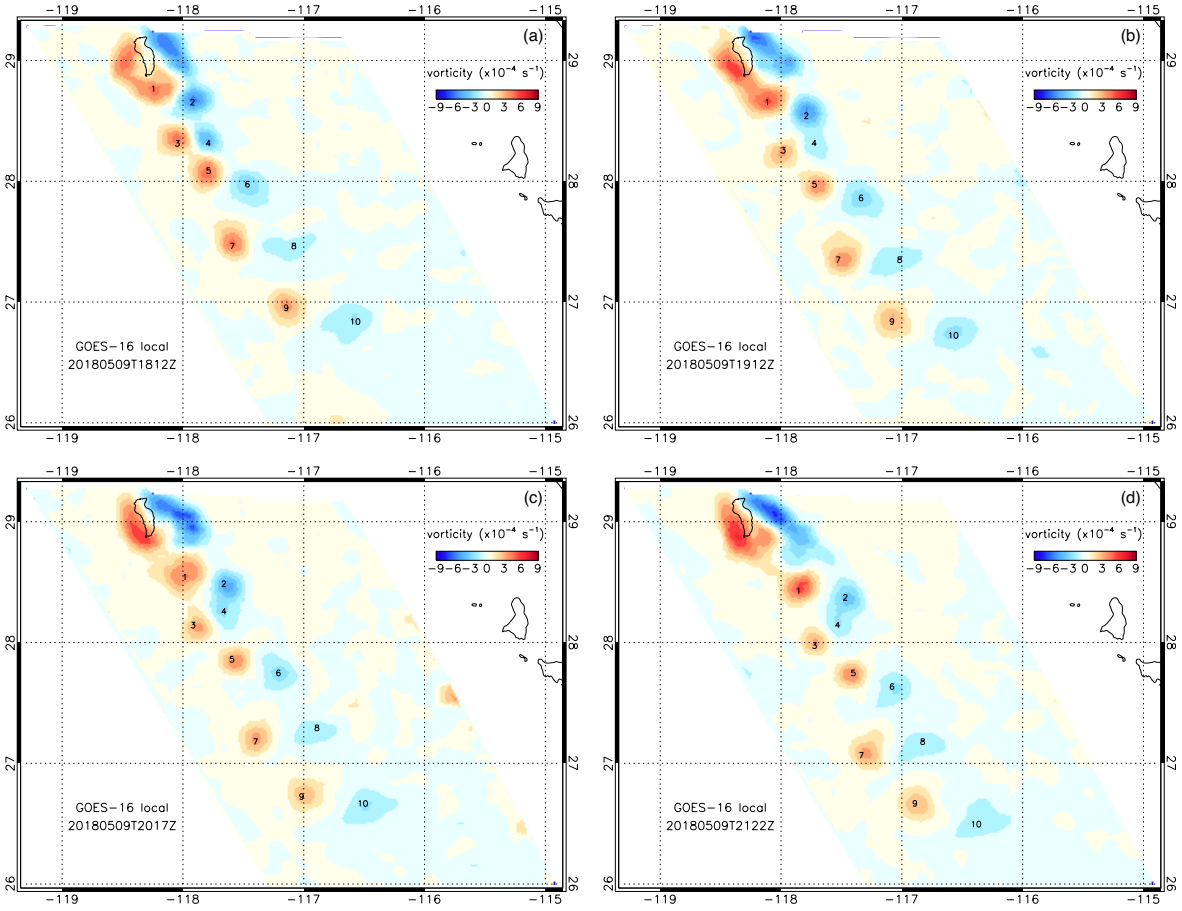

Figure 9. Same as Figure 6, but for the relative vorticity ζ smoothed with a 3×3-gridbox averaging window. The numbers mark the locations of vorticity minima or maxima of the ten vortices identified in Figure 4.

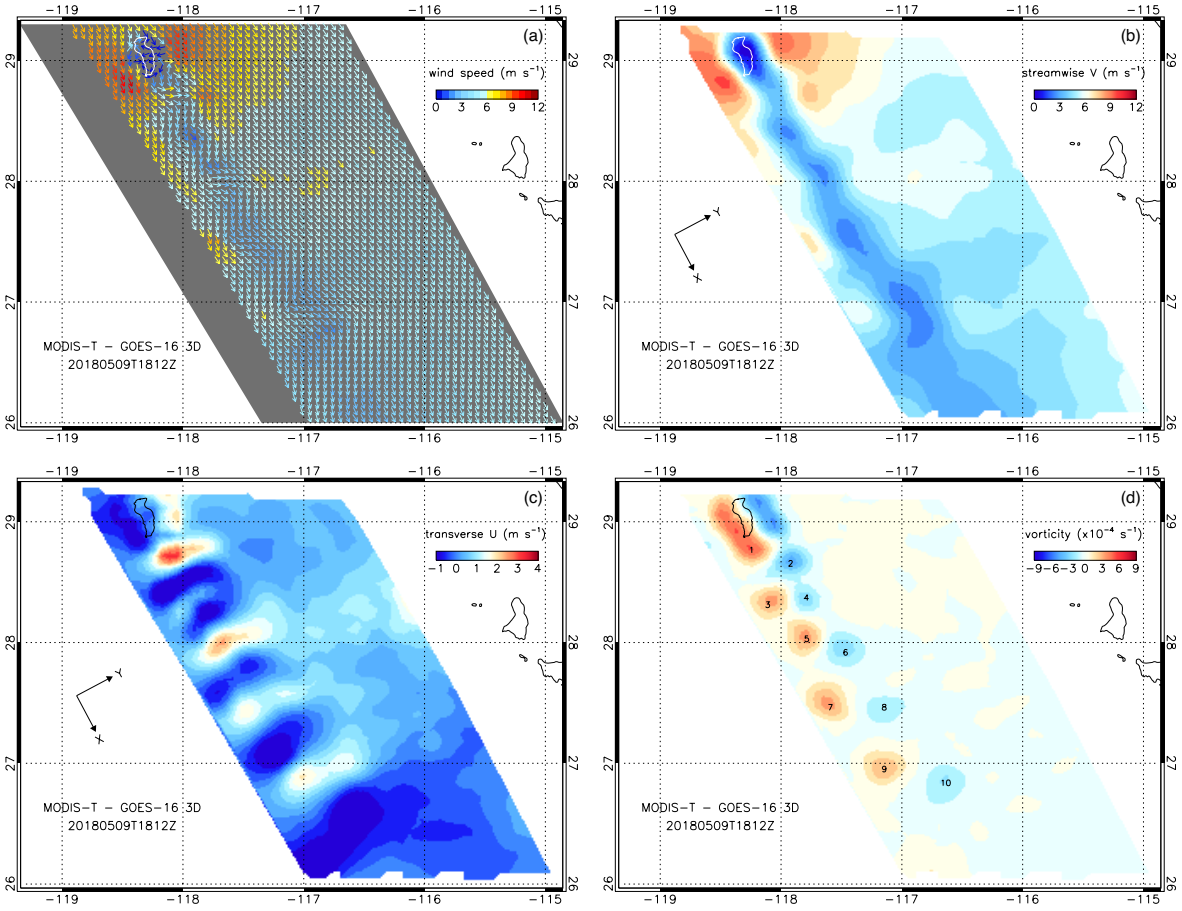

Figure 10. Median-filtered MODIS *Terra*–GOES-16 3D winds resampled on a 6.3-km UTM grid on 9 May 2018 at 1812Z: (a) wind vectors colored according to wind speed, (b) the streamwise wind component V, (c) the transverse wind component U, and (d) the relative vorticity. No smoothing was applied to the wind vectors in panel (a), but the data in panels (b,c, and d) were smoothed with a 3×3-gridbox averaging window. The numbers in panel (d) mark the locations of vorticity minima or maxima of the ten vortices identified in Figure 4. See Figures 6a, 7a, 8a, and 9a for comparison with the corresponding GOES-16 local winds.

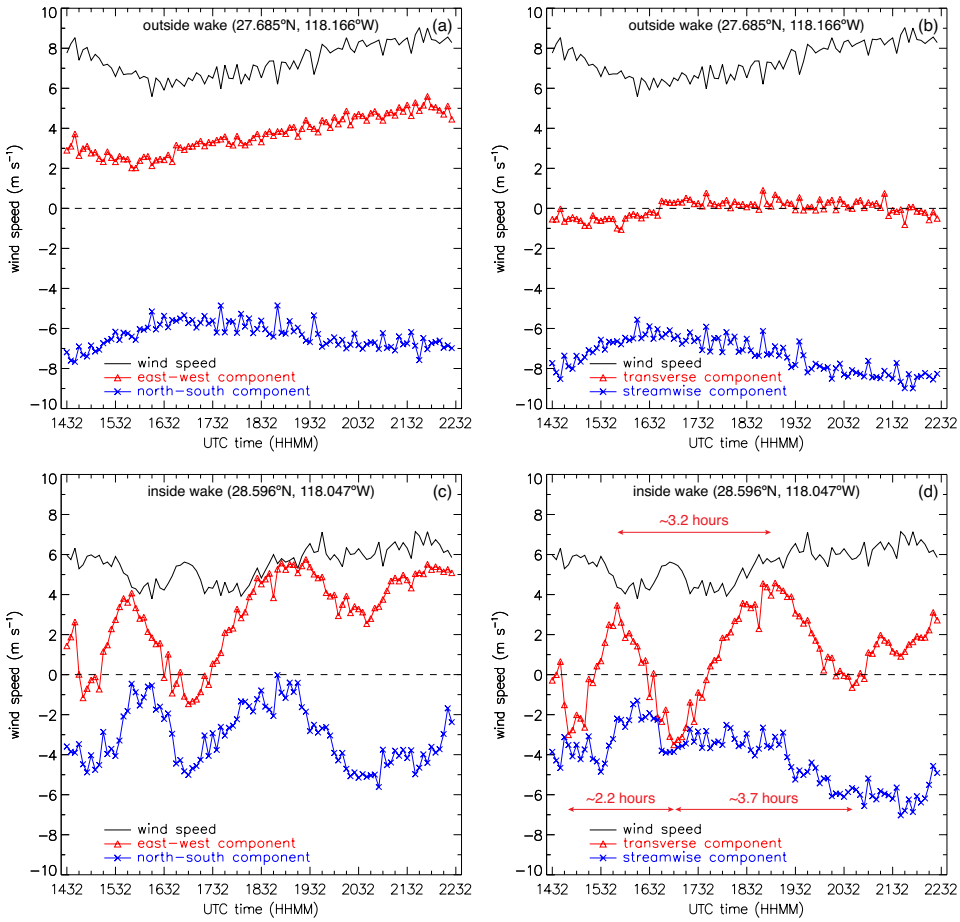

Figure 11. Temporal variation of GOES-16 local wind over an 8-hr period at 5-minute resolution and averaged for a 3×3-gridbox region (a and b) outside and (c and d) inside Guadalupe's wake. Panels (a and c) plot the N-S, E-W components, while panels (b and d) plot the streamwise, transverse components. In panel (d), the time intervals between the minima and maxima of the oscillating transverse wind are also indicated, which correspond to the shedding period T between two consecutive like-rotating vortices.

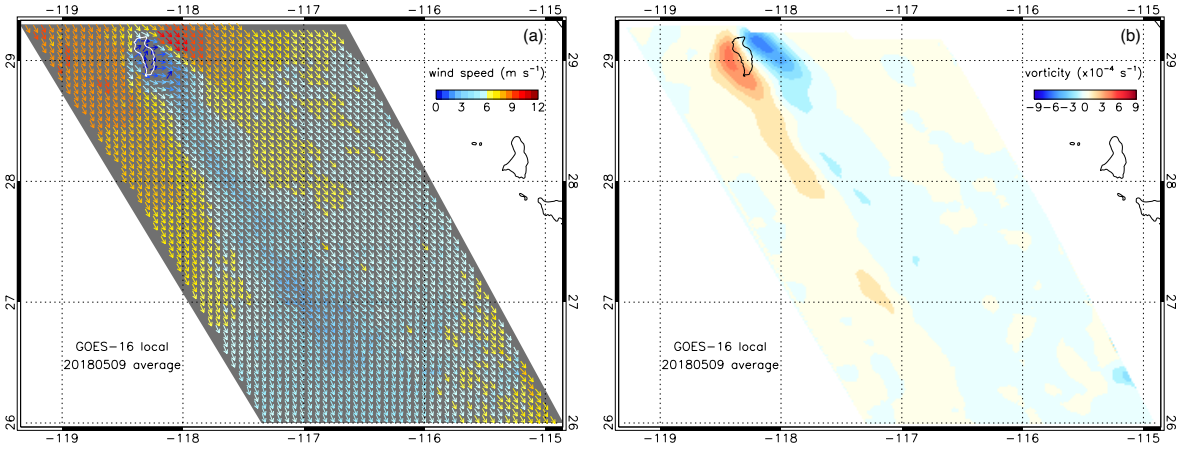

Figure 12. Time average of GOES-16 local winds over the 8-hr period between 14:37 and 22:32 UTC: (a) wind vectors and (b) relative vorticity. No smoothing was applied to the wind vectors, but the vorticity was smoothed with a 3×3-gridbox averaging window.

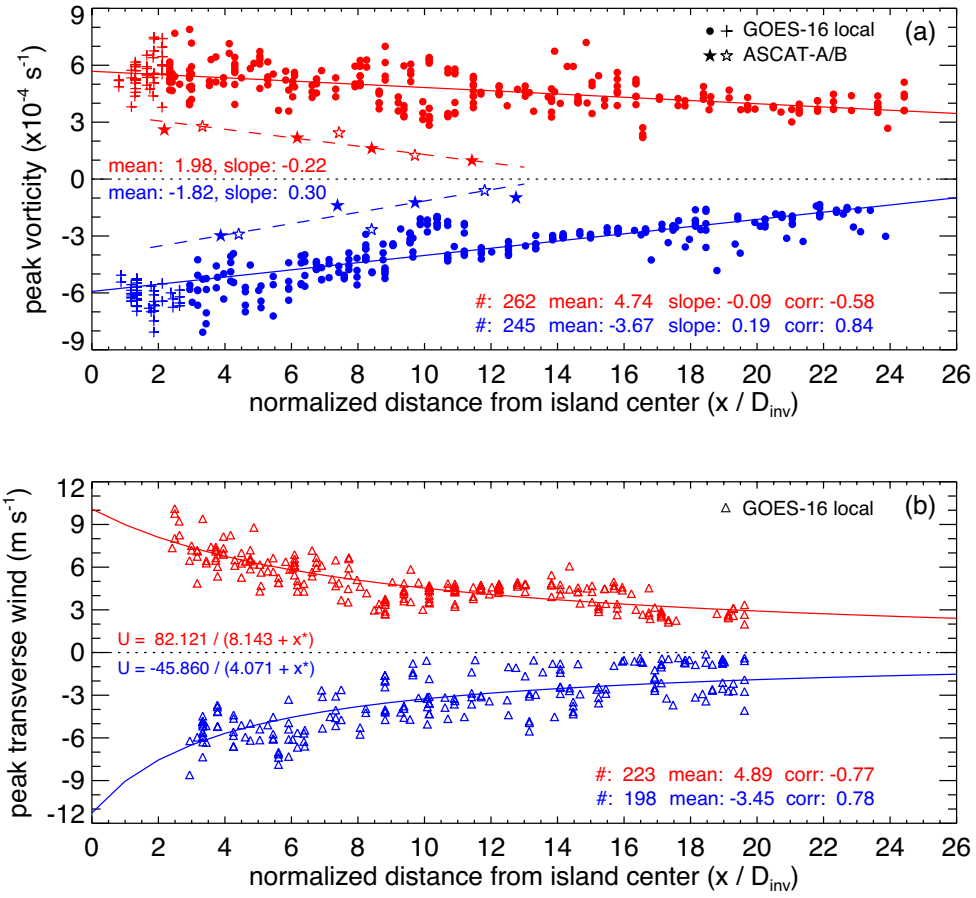

Figure 13. Decrease of (a) peak vorticity and (b) peak transverse wind in Guadalupe's wake as a function of normalized downstream distance $x^* = x/D_{inv}$ for cyclonic (red) and anticyclonic (blue) vortices. The GOES-16 local winds span the 5-hr period between 15:32 and 20:32 UTC, while the ASCAT-A/B surface winds correspond to the overpass times of 04:20 UTC and 05:20 UTC. The noisier vorticity data were smoothed with a 3×3-gridbox averaging window as before, but the transverse winds here are the raw unsmoothed values. In panel (a), the plus signs represent vorticity minima and maxima on the eastern and western flank of Guadalupe, while the filled circles represent the peak vorticity of individual downstream-advecting vortices tracked over time. The solid and dashed lines are linear fits to the downstream vorticity data. In panel (b), the solid curves are hyperbolic fits of the form $A / (B + x^*)$ to GOES-16 peak transverse winds. Note the statistical asymmetry between cyclonic and anticyclonic vortices, with the latter decaying faster than the former.

Table 1. Hourly meteorological conditions in the boundary layer upstream of Guadalupe on 9 May 2018. Inversion base height h_{inv} and the corresponding wind speed and wind direction are from ERA5. The angle of attack α is relative to the major axis of Guadalupe's "mass density" ellipse oriented at 343°. The height of the dividing streamline h_c is calculated from equation (2), while the crosswind island diameter at inversion base height D_{inv} is determined from the ASTER GDEM. The Froude number *Fr* and the Rossby number *Ro* are computed from equations (4) and (5).

UTC hour	Wind speed (m s^{-1})	Wind direction / α (degree)	h_{inv} (m)	h_c (m)	D_{inv} (km)	Fr	Ro
00	7.76	318° / 25°	354	796	19.85	0.387	5.51
01	8.17	316° / 27°	351	780	20.64	0.399	5.58
02	8.79	314° / 29°	351	762	21.35	0.413	5.81
03	9.18	313° / 30°	351	747	21.72	0.424	5.96
04[a]	9.32	311° / 32°	354	742	22.38	0.428	5.87
05[b]	9.70	311° / 32°	356	759	22.38	0.415	6.11
06	10.20	314° / 29°	357	781	21.31	0.398	6.75
07	10.44	318° / 25°	355	786	19.85	0.394	7.42
08	10.62	324° / 19°	571	781	13.49	0.398	11.10
09	10.55	327° / 16°	570	768	12.42	0.408	11.98
10	9.53	326° / 17°	351	748	16.75	0.424	8.02
11	9.08	328° / 15°	348	739	15.98	0.430	8.01
12	9.02	329° / 14°	347	753	15.57	0.420	8.17
13	9.74	329° / 14°	346	776	15.58	0.402	8.82
14[c]	10.13	331° / 12°	348	812	14.72	0.374	9.70
15[c]	10.38	334° / 09°	568	858	9.87	0.339	14.83
16[c]	10.21	334° / 09°	570	866	9.87	0.333	14.59
17[c]	9.95	334° / 09°	570	810	9.87	0.376	14.22
18[c]	9.80	332° / 11°	570	783	10.57	0.397	13.07
19[c]	9.60	330° / 13°	568	785	11.31	0.395	11.97
20[c]	9.61	328° / 15°	565	810	12.08	0.376	11.22
21[c]	9.79	327° / 16°	562	833	12.45	0.358	11.09
22[c]	8.98	322° / 21°	556	892	14.36	0.313	8.82
23	9.76	324° / 19°	553	899	13.63	0.307	10.10

[a] ASCAT-A wind retrievals
[b] ASCAT-B wind retrievals
[c] GOES-16 wind retrievals

Table 2. Vortex street geometry as defined in Figure 1 and calculated from the 0.25-km pixel resolution MODIS *Terra*, VIIRS *Suomi NPP*, and MODIS *Aqua* images shown in Figure 4. Results are given for the three southernmost vortex triplets t1 = (V6, V7, V8), t2 = (V7, V8, V9), and t3 = (V8, V9, V10). Bold italic numbers highlight geometric parameters for vortex triplet t3, which was least affected by the change in wind direction and wind speed and thus yielded the temporally most consistent aspect ratios. For comparison, Young and Zawislak (2006) obtained a mean aspect ratio of 0.42 with a 95% confidence interval of 0.36–0.47 for regular atmospheric vortex streets.

	H (km)			L (km)			H/L		
	t1	t2	t3	t1	t2	t3	t1	t2	t3
MODIS T	46.18	38.46	***36.84***	74.00	76.22	***84.39***	0.62	0.50	***0.44***
VIIRS	50.51	43.89	***40.97***	64.89	71.21	***89.10***	0.78	0.62	***0.46***
MODIS A	51.36	42.43	***35.75***	64.20	65.77	***85.59***	0.80	0.65	***0.42***

Table 3. Statistical comparison between MODIS–GOES-16 3D winds and GOES-16 local winds over the Guadalupe domain at the *Terra* and *Aqua* overpass times on 9 May 2018. The two separate wind products were median-filtered and resampled without smoothing on a common 6.3-km UTM grid, resulting in 3866 data pairs.

	Absolute / Relative Bias ($m\ s^{-1}$ / %)	RMSD ($m\ s^{-1}$)	Correlation
Wind speed	0.12 / 2.20	0.72	0.92
E-W component	0.05 / 1.50	0.82	0.86
N-S component	-0.21 / 4.90	0.92	0.85

Table 4. Statistical summary of downstream vorticity ζ plotted in Figure 13a. Here $x^* = x/D_{inv}$ is the normalized downstream distance.

	Mean ($\times 10^{-4}\ s^{-1}$)	Median ($\times 10^{-4}\ s^{-1}$)	Correlation (ζ, x^*)	Slope ($\times 10^{-4}\ s^{-1}$ / D_{inv})	Slope ($\times 10^{-4}\ s^{-1}$ / 100 km)	Count
GOES-16 +	4.74	4.65	-0.58	-0.086	-0.806	262
GOES-16 -	-3.67	-3.47	0.84	0.190	1.792	245
ASCAT +	1.98	2.17	-0.93	-0.222	-0.993	7
ASCAT -	-1.82	-1.39	0.93	0.298	1.331	7